



RESEARCH ARTICLE

10.1029/2021MS002814

CMIP6 Simulations With the CMCC Earth System Model (CMCC-ESM2)

Key Points:

- This work introduces the second generation CMCC Earth System Model (CMCC-ESM2) and its configuration for CMIP6
- Estimated climate sensitivity and carbon-climate feedbacks are similar to average of CMIP5 and locate in the lower end of CMIP6
- Both climate and biogeochemical dynamics are assessed through the comparison with observations and previous literature findings

Supporting Information:

Supporting Information may be found in the online version of this article.

Correspondence to:

T. Lovato,
tomas.lovato@cmcc.it

Citation:

Lovato, T., Peano, D., Butenschön, M., Materia, S., Iovino, D., Scoccimarro, E., et al. (2022). CMIP6 simulations with the CMCC Earth System Model (CMCC-ESM2). *Journal of Advances in Modeling Earth Systems*, 14, e2021MS002814. <https://doi.org/10.1029/2021MS002814>

Received 15 SEP 2021

Accepted 4 FEB 2022

Author Contributions:

Conceptualization: T. Lovato, D. Peano, M. Butenschön, A. Navarra

Data curation: T. Lovato, D. Peano, P. G. Fogli

Formal analysis: T. Lovato, D. Peano, M. Butenschön

Funding acquisition: S. Gualdi, S. Masina

Investigation: T. Lovato, M. Butenschön, S. Materia, D. Iovino, E. Scoccimarro, A. Cherchi, A. Bellucci, S. Gualdi, S. Masina, A. Navarra

T. Lovato¹ , D. Peano¹ , M. Butenschön¹ , S. Materia¹ , D. Iovino¹ , E. Scoccimarro¹ , P. G. Fogli¹ , A. Cherchi^{1,2} , A. Bellucci^{1,2} , S. Gualdi¹ , S. Masina¹ , and A. Navarra^{1,3}

¹Fondazione Centro Euro-Mediterraneo sui Cambiamenti Climatici, CMCC, Bologna, Italy, ²Now at National Research Council, Institute of the Atmospheric Sciences and Climate (CNR-ISAC), Bologna, Italy, ³Department of Biological, Geological and Environmental Sciences (BIGEA), Università di Bologna, Bologna, Italy

Abstract This article introduces the second generation CMCC Earth System Model (CMCC-ESM2) that extends a number of marine and terrestrial biogeochemical processes with respect to its CMIP5 predecessor. In particular, land biogeochemistry was extended to a wider set of carbon pools and plant functional types, along with a prognostic representation of the nitrogen cycle. The marine ecosystem representation was reshaped toward an intermediate complexity of lower trophic level interactions, including an interactive benthic compartment and a new formulation of heterotrophic bacterial population. Details are provided on the model setup and implementation for the different experiments performed as contribution to the sixth phase of the Coupled Model Intercomparison Project. CMCC-ESM2 shows an equilibrium climate sensitivity of 3.57°C and a transient climate response of 1.97°C which are close to the CMIP5 and CMIP6 multi-model averages. The evaluation of the coupled climate-carbon response in the historical period against available observational datasets show a consistent representation of both physical and biogeochemical quantities. However, the land carbon sink is found to be weaker than the current global carbon estimates and the simulated marine primary production is slightly below the satellite-based average over recent decades. Future projections coherently show a prominent global warming over the northern hemisphere with intensified precipitations at high latitudes. The expected ranges of variability for oceanic pH and oxygen, as well as land carbon and nitrogen soil storage, compare favorably with those assessed from other CMIP6 models.

Plain Language Summary Earth System Models integrate our knowledge on the underlying physical and biogeochemical mechanisms that drive or influence the global climate and the biosphere over the land and in the ocean. These models are used to provide realistic estimates of climate variability and its response to perturbations in the chemical constituents of the atmosphere and modifications of the terrestrial surface. This work describes the science at the base of the second generation Earth System Model developed at the Euro-Mediterranean Centre on Climate Change and the major results obtained from the simulation of historical (from the pre-industrial period until present) and different future scenarios up to 2100 in the context of the sixth Coupled Model Intercomparison Project. The model provides a solid representation of the present-day physical climate and biosphere dynamics in comparison to available observations and data reconstruction of the recent past. The projected global warming signal and carbon accumulation within terrestrial and oceanic systems under future climate scenarios are comparable to the findings of other models involved in the sixth intercomparison project.

1. Introduction

The Euro-Mediterranean Centre on Climate Change (CMCC) Foundation has contributed to the Coupled Model Intercomparison Project (CMIP) since its early stages, as the research on climate evolution and global biogeochemical cycles is a strategic pillar to ensure the maintenance of a healthy equilibrium between our planet and ourselves (CMCC, 2020). Since the atmosphere-ocean coupled model SINTEX-G used in CMIP3 (Gualdi et al., 2008), CMCC has worked on the development of both Climate and Earth System Models, namely CMCC-CM (Scoccimarro et al., 2011) and CMCC-CESM (Vichi et al., 2011), which were part of the fifth CMIP phase (CMIP5; Taylor et al., 2012). This continued effort led to the development of a new generation of global coupled models to respond to different needs and applications for the CMIP6 climate research, which is here specifically addressed to the coupled climate-carbon cycle dynamics resolved by the CMCC Earth System Model version 2 (CMCC-ESM2).

© 2022 The Authors. *Journal of Advances in Modeling Earth Systems* published by Wiley Periodicals LLC on behalf of American Geophysical Union. This is an open access article under the terms of the [Creative Commons Attribution License](https://creativecommons.org/licenses/by/4.0/), which permits use, distribution and reproduction in any medium, provided the original work is properly cited.

Methodology: T. Lovato, E. Scoccimarro, A. Cherchi, A. Bellucci

Resources: S. Gualdi, S. Masina, A. Navarra

Software: P. G. Fogli

Supervision: S. Gualdi, S. Masina, A. Navarra

Visualization: T. Lovato, D. Peano

Writing – original draft: T. Lovato, D. Peano, M. Butenschön, S. Materia, E. Scoccimarro, A. Cherchi, A. Bellucci, S. Gualdi, S. Masina, A. Navarra

Writing – review & editing: T. Lovato, D. Peano, M. Butenschön, S. Materia, D. Iovino, E. Scoccimarro, P. G. Fogli, A. Cherchi, A. Bellucci

CMCC-ESM2 uses the physical-dynamical core of its atmosphere-ocean general circulation model counterpart, named CMCC-CM2 (Cherchi et al., 2019), and accounts for the Earth system feedbacks enabled by the interactive land and ocean biogeochemical processes as simulated by the Community Land Model (Oleson et al., 2013) and the Biogeochemical Flux Model (BFM v5.2; Vichi et al., 2020), respectively. With respect to the previous CMCC-CESM model, these biogeochemical components present substantial advancements (details in Section 2). Overall, the land component account for a wider ensemble of vegetation types and carbon pools along with the prognostic representation of the nitrogen cycle. Marine biogeochemistry is resolved for an intermediate complexity ecosystem structure, with explicit heterotrophic bacteria, and includes an interactive benthic compartment.

The aims of this paper are to present the main characteristics of the CMCC-ESM2 in the context of CMIP6 coordinated experiments and to evaluate the model's ability in reproducing the coupled climate-carbon cycle interactions under present-day and future climate conditions. In particular, we included in our analyses a set of metrics consolidated by recent studies tackling the main climate and carbon-related biogeochemical processes within CMIP6 (Arora et al., 2020; Jones & Friedlingstein, 2020; Kwiatkowski et al., 2020; Meehl et al., 2020; Séférian et al., 2020; Tebaldi et al., 2021).

Section 2 provides a brief description of the model components, along with the spin-up strategy following the CMIP6 protocols, and the description of the DECK and ScenarioMIP simulations performed using CMCC-ESM2. In Section 3, main climate sensitivity metrics and coupled climate-carbon feedbacks are presented and discussed, along with the analysis of relevant global scale physical quantities simulated under present and future climate scenarios. Moreover, key biogeochemical processes within terrestrial and ocean components are addressed to evaluate the model performance against available present-day observations and to describe the projected long-term marine and terrestrial ecosystems response. In the final section, the main outcomes of the analysis are summarized and concluding remarks are drawn.

2. CMCC-ESM2 Model Description and CMIP6 Simulations

2.1. Model Configuration

The reference CMIP6 configuration of CMCC-ESM2 has an atmospheric horizontal resolution of about 1° , with a regular grid of $0.9^\circ \times 1.25^\circ$ in latitude and longitude, while in the vertical it accounts for 30 layers up to 2 hPa with a hybrid sigma-pressure coordinate (spacing between layers of 1.2 Km). The land component employs the same horizontal grid as the atmosphere and the vertical soil structure is represented by 15 layers down to the depth of 42 m, while hydrology calculations are performed over the top 10 layers, down to 3.8 m (Oleson et al., 2013). For the ocean, a tripolar system from the ORCA family (Madec & Imbard, 1996) is used. It corresponds to a nominal resolution of 1° , with a finer meridional spacing near the Equator. In the vertical dimension 50 geopotential levels are considered, ranging from 1 m at the surface to 400 m of thickness in the deep ocean. The horizontal grid of the oceanic model is used by the sea ice component that explicitly resolves the sea ice state over five different thickness categories. This configuration represents a substantial upgrade in comparison to the previous one of CMCC-CESM, which used an horizontal grid with a resolution of 3.75° for the atmospheric and land components and 2° for the oceanic and sea ice components.

Only a brief summary of the CMCC-ESM2 physical core is presented in the following section, as a detailed description of the system is given in Cherchi et al. (2019) for the companion atmosphere-ocean general circulation model CMCC-CM2-SR5. In this work, a more detailed description of the terrestrial and marine biogeochemistry is offered since these components represent the main advancements with respect to the CMIP5 model version, namely CMCC-CESM (Vichi et al., 2011).

2.1.1. Physical Core

The physical core comprises three-dimensional dynamical models for the atmosphere, ocean (including sea-ice), and land communicating via a coupler (CPL v7; Craig et al., 2012) that handles the exchange of fields among the different model components.

The atmospheric model is based on the finite-volume dynamical core of the Community Atmosphere Model (CAM v5; Neale et al., 2012), which uses a three lognormal modes implementation of the modal aerosols module to simulate aerosol physical, chemical and optical properties (MAM3; Liu et al., 2012). For the terrestrial component, the Community Land Model (CLM v4.5; Oleson et al., 2013) is coupled to provide boundary conditions

to the atmosphere and freshwater input into the ocean (more details on biogeochemical processes in the next section). The ocean general circulation is simulated by the European community model NEMO (v3.6; Madec & the NEMO System team, 2016) that also solves the transport of oceanic tracers. For sea ice, the Community Ice CodE (CICE v4; Hunke et al., 2008) provides interactive sea ice properties based on ocean surface and atmospheric near-surface conditions. A thorough description of the adopted numerical schemes and parameterizations for the physical core of the model is given in Cherchi et al. (2019).

2.1.2. Terrestrial Biogeochemistry

The terrestrial biogeochemistry processes in CMCC-ESM2 are represented by the Community Land Model version 4.5 (Oleson et al., 2013) in its biogeochemical (BGC) configuration (Koven et al., 2013) that covers the main processes relevant to global carbon and nitrogen cycles.

The photosynthesis description differs among the plant types (Bonan et al., 2011), as plants whose first product of photosynthesis is a 3-carbon molecule (C3 plants) are represented by the Farquhar et al. (1980) model, while those with 4-carbon molecule as initial photosynthetic product (C4 plants) are simulated with the method of Collatz et al. (1992). The main difference between these two methods resides in the leaf-level parameterization of the carboxylation and its limiting factors (e.g., Rubisco and PEP activity thresholds, light- and product-limited rates). The photosynthate is then allocated into vegetation carbon pools: leaf, live stem, dead stem, live coarse root, dead coarse root, and fine root. The transfer of vegetation carbon into litter-soil pools is described as a transformation dynamical cascade going from coarse woody debris to litter and soil organic matter pools. The decomposition cascade is based on the Century model (Parton et al., 1988). During the decomposition cascade, a fraction of carbon is released into the atmosphere as CO₂, named respiration fraction. The respiration fraction is estimated using multiple exponential models fitted to data from the results of microcosm decomposition experiments (Thornton, 1998) and the time-evolution of the vegetation spatial distribution is prescribed using 15 plant functional types (PFTs). While land cover is prescribed, the seasonality of plant growth and litterfall (i.e., plant phenology) is prognostic and responds to soil and air temperature, soil moisture, and day length (Oleson et al., 2013; Peano et al., 2019, 2021). CLM4.5-BGC contains a fire module that describes four components: non-peat fires outside cropland and tropical closed forests, agricultural fires, deforestation fires in the tropical closed forests, and peat fires. In the fire module, the burned area is estimated based on climate conditions, vegetation composition and structure, and human activities, as reported in Li et al. (2012a, 2012b, 2013).

The carbon cycle implemented in the land surface scheme of the previous CMCC-ESM2, named SILVA (Alessandri, 2006), was based on parameterizations from the VEgetation-Global-Atmosphere-Soil (VEGAS; Zeng et al., 2005) model. CLM4.5-BGC brings a wide set of enhancements compared to VEGAS, as (a) the number of carbon pools used in representing the allocation of carbon in vegetation is doubled, (b) the decomposition cascade extends to coarse woody debris and three litter pools (namely fast, intermediate, and slow) along with the three main soil pools (namely fast, intermediate, and slow), and (c) a significant increase in the vegetation heterogeneity by using 15 PFTs versus 4 PFTs used in VEGAS.

The main improvement in terrestrial biogeochemistry introduced in CMCC-ESM2 with respect to the previous version is the prognostic representation of the nitrogen cycle. The external inputs of mineral nitrogen are from atmospheric deposition and biological nitrogen fixation (BNF). The former accounts for wet and dry deposition of reduced and oxidized forms as a single flux (Bertolini et al., 2016), which is provided as a spatially and temporally varying data set (Table 1). The BNF from atmospheric gaseous nitrogen mediated by soil microorganisms is described as a function of net primary production (Cleveland et al., 1999), similar to other terrestrial biogeochemistry models employed in CMIP6 (see Davies-Barnard et al., 2020). The nitrogen retrieved from the atmosphere is then stored in the soil mineral nitrogen pool, where plant and heterotrophic communities compete for their demand for the element. The fraction of nitrogen up-taken by plants is allocated into vegetation nitrogen pools (namely leaf, live stem, dead stem, live coarse root, dead coarse root, and fine root) based on static carbon to nitrogen ratios defined on tissue types and PFT (Larcher, 1995; Oleson et al., 2013). Losses of mineral nitrogen result from nitrification, denitrification, leaching, and fire losses. In particular, the representation of nitrification and denitrification is based on the Century Nitrogen model (Del Grosso et al., 2000; Parton et al., 1996, 2001): nitrification of ammonia is described as a function of temperature, moisture, and pH, while the potential denitrification rate is co-limited by nitrate concentration and carbon consumption rates and occurs only in the anoxic fraction of soils. Besides, fluxes of nitrous oxide are simulated through a “hole-in-the-pipe” approach (Firestone & Davidson, 1989), with leaching losses depending on the concentration of dissolved mineral nitrogen in soil water

Table 1
DECK and ScenarioMIP Concentration Driven Simulations Characteristics and Forcing Fields

	Duration (years)	Greenhouse gases concentrations	Anthropogenic aerosols emissions	Land use	Ozone	Nitrogen deposition
piControl	500	CO ₂ = 284.32 ppm CH ₄ = 808.25 ppb N ₂ O = 273.02 ppb CFC-11eq = 32.11 ppt	As in historical, fixed to 1850	As in historical, fixed to 1850	As in historical, fixed to 1850	As in historical, fixed to 1850
Historical	165	UoM-CMIP v1.2	CEDS 2017-08-30	UofMD-landState high v2.1 hr	UReading-CCMI v1.0	NCAR-CCMI v2.0
ssp126	85	UoM-IMAGE v1.2	IAMC-IMAGE v1.1	UofMD-landState IMAGE-ssp126 v2.1f	UReading-CCMI v1.0	NCAR-CCMI v1.0
ssp245	85	UoM-MESSAGE-GLOBIOM v1.2	IAMC-MESSAGE-GLOBIOM v1.1	UofMD-landState MESSAGE-ssp245 v2.1f	UReading-CCMI v1.0	NCAR-CCMI v1.0
ssp370	85	UoM-AIM v1.2	IAMC-AIM v1.1	UofMD-landState AIM-ssp370 v2.1f	UReading-CCMI v1.0	NCAR-CCMI v1.0
ssp585	85	UoM-REMIND-MAGPIE v1.2	IAMC-REMIND-MAGPIE v1.1	UofMD-landState MAGPIE-ssp585 v2.1f	UReading-CCMI v1.0	NCAR-CCMI v1.0

Note. 1pctCO₂, 1pctCO₂-bgc, and abrupt-4xCO₂ are not listed as these experiments share the same bulk forcing of piControl, aside from CO₂ concentration idealized evolution. Two datasets are common to all experiments: Solar forcing from SOLARIS-HEPPA v3.2 (Matthes et al., 2017), and stratospheric aerosol forcing from IACETH-SAGE v3 (ETH Zürich, 2017) applied following CMIP6 protocols (Eyring et al., 2016; O'Neill et al., 2016). Data set references: UoM-CMIP (Meinshausen & Vogel, 2016), CEDS 2017-08-30 (Hoesly et al., 2016), UReading-CCMI (Hegglin et al., 2016), NCAR-CCMI (Hegglin et al., 2018), and UofMD-landState (Hurt et al., 2019). IAMC-scenario emissions (Gidden et al., 2018) and UoM-greenhouse gases concentrations (Meinshausen & Nicholls, 2018).

solution and the rate of hydrologic discharge on the soil column to streamflow. Note that CLM4.5-BGC assumes that a constant fraction of the soil mineral nitrogen pool is in soluble form and acts only on the nitrate pool. The loss of nitrogen through fire instead is determined by the fraction of biomass lost to combustion. Finally, the availability of mineral nitrogen also limits the decomposition rates in the carbon decomposition cascade.

2.1.3. Marine Biogeochemistry

The ocean biogeochemical component of CMCC-ESM2 is based on the BFM v5.2 (Vichi et al., 2020) that solves the cycles of major chemical constituents in the lower trophic levels through a variable stoichiometric composition of both living functional groups and non-living marine compounds. The main differences from the previous CMCC-CESM model reside in the application of a more compact pelagic ecosystem structure and the inclusion of an interactive benthic compartment for the remineralization of organic sediments.

The configuration adopted for CMIP6 is of intermediate complexity, having a total of 32 pelagic and 14 benthic prognostic state variables (Table A1), where the lower level ecosystem dynamics are determined by the interplay between heterotrophic bacteria, two phytoplanktonic (diatoms and nano-flagellates) and two zooplanktonic (micro- and meso-zooplankton) functional groups. This revised pelagic network (the previous model used 54 state variables) retains the ecosystem interactions between major functional groups and introduces novel biogeochemical dynamics, while being on a practical level a computationally tractable model for climate applications. In this configuration, bacterial and zooplanktonic groups are modeled in terms of the sole carbon constituent and their biogeochemical dynamics are driven by fixed stoichiometric ratios. Other chemical functional families included in the model are nitrate, ammonium, orthophosphate, silicate, dissolved bioavailable iron, oxygen, and dissolved and particulate (non-living) organic matter (DOM and POM).

The ocean carbonate system is resolved using dissolved inorganic carbon (DIC) and total alkalinity (TA) as prognostic variables and formulations for the atmosphere–ocean gas exchange and carbon chemistry follow the protocol guidelines of the Ocean Model Intercomparison Project biogeochemical stream (OMIP-BGC; Orr et al., 2017), with carbon chemistry constants recommended for best practices (Dickson, 2010) on the total pH scale. In addition, the BFM was set to use in-situ temperature and vertical pressure values, as recommended in Orr et al. (2015). Beside the air-sea exchanges and riverine loads, the evolution of DIC and TA is also determined by changes in inorganic dissolved nitrogen and calcite (CaCO₃), where calcite production is linearly

dependent on nanophytoplankton carbon production with a constant ratio of inorganic to organic particulate carbon concentrations.

Ocean pelagic biogeochemistry was here extended by including new processes for the cycling of chemical constituents within organic matter pools and for the growth of heterotrophic bacteria. In particular, the external inputs of iron and its remineralization within both dissolved and particulate organic matter was modified to account for relevant missing processes, as highlighted in the CMIP5 FeMIP intercomparison exercise of Tagliabue et al. (2016). A remarkable drawback of the previous CMCC-CESM model is represented by the large dissolved oxygen negative drifts occurring in sub-surface and intermediate ocean depths over long time scales (see Séférian et al., 2016). The reduction of dissolved oxygen concentrations simulated in the ocean interior is primarily reconducible to bacterial respiration rates driven by a too high uptake of sinking organic matter. Based on the heterotrophic bacteria parameterization for global ocean applications (BACT1 in Vichi et al., 2020), the growth-related dynamics were revised by considering two distinct population behaviors when bacterial biomass is associated with either DOM or POM. In the first case, the growth is governed by a combined dependence from temperature and substrate accessibility, while on particulate organic matter bacteria form attached colonies that primarily grow according to the substrate availability. In the same way, the organic matter by-products of bacterial activity are returned to the associated substrate. The combination of these targeted design choices allows for an improved and more efficient representation of the core ecosystem functions relevant to the Earth System dynamics. A detailed description of these extended BFM features developed for CMIP6, along with choices for model parameterizations, can be found in Appendix A.

2.2. CMIP6 Simulations and Data Distribution

The focus of this work is the analysis of the DECK and ScenarioMIP concentration-driven simulations that were performed according to the CMIP6 reference protocols (Eyring et al., 2016; O'Neill et al., 2016), whose key characteristics and forcing fields are summarized in Table 1. In addition, CMCC-ESM2 was also used to perform numerical experiments supporting the research activities of C⁴MIP (Lovato et al., 2021), LS3MIP (Peano et al., 2020a), LUMIP (Peano et al., 2020b), and OMIP (Lovato & Butenschön, 2021) intercomparison projects.

The final state achieved at the end of the spin-up procedure, detailed in the following section, represents the branching point for the pre-industrial (piControl), historical, and idealized greenhouse gas forcing (1pctCO₂ and abrupt-4xCO₂ of DECK, 1pctCO₂-bgc of C⁴MIP) simulations. At the end of the historical simulation in year 2014, the scenario simulations are initiated prescribing the pertaining forcing derived from the Shared Socioeconomic Pathways (Meinshausen et al., 2020). Simulations were branched off sufficiently long before the end of the piControl simulation to ensure the year-to-year data correspondence necessary to compute the climate drift in the perturbed simulation, as recommended in Eyring et al. (2016). All data produced within the different experiments were standardized using the CMIP6 Data Request v1.00.31 catalog (Jukes et al., 2020) and are made available through a dedicated data node of the Earth System Grid Federation infrastructure supported by the CMCC Super-Computing Center (details at www.cmcc.it/super-computing-center-scc).

2.3. CMCC-ESM2 Initialization and Spin-Up

The achievement of an equilibrated state for an Earth System Model under pre-industrial conditions is a desirable prerequisite to perform reliable present and future climate simulations. To reach such a balance in coupled climate-carbon cycles and reduce residual drifts, models are spun-up over long time scales by exploiting a variety of techniques (see e.g., Séférian et al., 2020).

Here, a sequential procedure was adopted for the concentration-driven spin-up of CMCC-ESM2 by first realizing the adjustment of carbon pools for both land and ocean components over long timescales in a decoupled mode, followed by the equilibration of the fully coupled model under pre-industrial forcing conditions.

The land carbon and nitrogen pools were initialized using the two phases method described by Koven et al. (2013) under prescribed atmospheric fields over the period 1901–1930 obtained from the Global Soil Wetness Project Phase 3 (Kim, 2017). An initial accelerated simulation of 1,020 years was used to reach an approximate annual turnover timescale for both pools, which was followed by a 300-year-long simulation without any acceleration to reinstate each pool in its original turnover timescale.

Table 2
Global Mean Values and Drift Rates for a Set of Climatic and Biogeochemical Key Properties Computed From the Last 100 Years of CMCC-ESM2 Coupled Spin-Up Simulation

Variable	Units	Mean	Drift (ky ⁻¹)
Air temperature at 2 m	°C	13.73	0.04
Top-of-atmosphere radiation balance	W m ⁻²	0.64	-0.78
Leaf Area Index	–	1.53	-0.23
Total Land Carbon Content	PgC	3,434.79	-4.87
Seawater surface temperature	°C	17.90	0.47
Seawater surface salinity	0.001	34.19	-1.03
Surface dissolved oxygen	mmol m ⁻³	249.94	0.18
Surface dissolved inorganic nitrogen	mmol m ⁻³	4.73	-1.41
Surface dissolved inorganic phosphorus	mmol m ⁻³	0.39	-0.35
Surface dissolved inorganic carbon	umol kg ⁻¹	1,996.04	-4.82
Surface total alkalinity	umol-eq kg ⁻¹	2,311.43	-6.76

Note. Drift rates were calculated as the linear fit of annual mean values across the considered period and are shown as ky⁻¹. A companion table reporting the same statistics for the 500 year-long piControl experiment is provided in the supplementary material (Table S1 in Supporting Information S1).

Initial conditions for the ocean biogeochemistry were set in agreement with the OMIP-BGC protocols (Orr et al., 2017) and forcing fields for nitrogen deposition and atmospheric carbon dioxide were fixed to the year 1,850 reference values. Climatological river loads were set using estimates from Mayorga et al. (2010). This component was spun up for 300 years in offline mode forced by dynamical fields obtained from the first 10 years of the CMCC-CM2-SR5 piControl simulation (Lovato & Peano, 2020).

In the final step of the procedure, CMCC-ESM2 started from the combination of the physical state at the beginning of the CMCC-CM2-SR5 piControl run with the final conditions obtained in the individual land and ocean spin-ups. The fully coupled model performed a 425 year long simulation with forcing fields prescribed to 1,850 reference conditions for greenhouse gas concentrations, ozone concentration, surface land conditions, nitrogen deposition, and background volcanic aerosol (see piControl in Table 1).

As a perfect equilibrium in a spin-up simulation is generally hard to achieve, a set of relevant climatic and biogeochemical properties were incrementally computed to evaluate when the model reaches a satisfactory balanced condition. Changes over the last simulated century are summarized in Table 2. The global mean 2-m air temperature is close to the expected pre-industrial value with a contained drift, although the radiation balance at the top of the atmosphere is rather high thus leading to a tendency of the surface ocean toward a warmer state (Loeb et al., 2012). The rather small drift achieved here for marine biogeochemical properties is an important prerequisite for the production runs, as it implies more reliable feedbacks from the biogeochemical cycles (Séférian et al., 2016). Land vegetation and carbon store evolution are also characterized by low drift values.

The model reaches a net land carbon flux into the atmosphere equal to -0.02 PgC y^{-1} ($<0.1 \text{ PgC y}^{-1}$, Eyring et al., 2016), land carbon store drift is far smaller than 10 PgC/century (Jones et al., 2016), and the air-sea CO₂ flux drift is $\sim 0.001 \text{ PgC y}^{-1}$, thus satisfying the $<0.01 \text{ PgC y}^{-1}$ criterion suggested by the OMIP-BGC protocol (Orr et al., 2017).

3. Results and Discussions

3.1. Climate Sensitivity and Climate-Carbon Feedbacks

The response of the global mean temperature to climate forcing, in particular to carbon dioxide concentrations, represents a key factor of uncertainty in future climate change projections (Nijssen et al., 2020). Such uncertainty in the climatic response can be estimated through a set of consolidated metrics that express the model sensitivity over different timescales.

Table 3

Climate Sensitivity and Carbon Feedback Metrics Diagnosed at CO₂ Doubling for CMCC-ESM2 Idealized Experiments (1pctCO₂, 1pctCO₂-bgc, and abrupt-4xCO₂) and for CMIP5 and CMIP6 Multi-Model Mean and Standard Deviation

	ECS (°C)	TCR (°C)	$\bar{E}_2 \times \text{CO}_2$ (PgC)	TCRE (°C EgC ⁻¹)	α (°C ppm ⁻¹)	β (PgC ppm ⁻¹)	γ (PgC °C ⁻¹)
CMCC-ESM2	3.57	1.97	947	1.79	0.0060	1.38	-20.76
CMIP5	3.2 ± 0.7	1.8 ± 0.4	1,021 ± 73	1.63 ± 0.48	0.0069 ± 0.0010	2.08 ± 0.62	-51.23 ± 29.34
CMIP6	3.7 ± 1.1	2.0 ± 0.4	1,093 ± 154	1.77 ± 0.37	0.0069 ± 0.0015	2.13 ± 0.43	-42.69 ± 39.43

Note. CMIP data for ECS and TCR are from Meehl et al. (2020); TCRE and cumulative CO₂ emissions ($\bar{E}_2 \times \text{CO}_2$) from Arora et al. (2020); linear transient climate sensitivity to CO₂ (α), carbon-concentration (β), and carbon-climate (γ) feedback metrics from Jones and Friedlingstein (2020). Note that TCRE is in units of °C per Exagram of carbon (1 EgC = 1,000 PgC).

The equilibrium climate sensitivity (ECS) measures the long-term response of global mean temperature that would occur if the atmospheric carbon dioxide concentration was doubled, while the transient climate response (TCR) addresses the warming amount over few decades by considering the transient response of global mean temperature at the time of CO₂ doubling relative to the pre-industrial state. Here, ECS is computed using the Gregory method (Gregory et al., 2004) by considering the climate response in the first 150 years of the abrupt-4xCO₂ experiment. TCR is determined as the mean global warming predicted to occur when CO₂ doubles in the 1pctCO₂ experiment, namely between years 61 and 80 from the beginning of the experiment (Gregory & Forster, 2008). These climate sensitivity metrics were estimated from the CMCC-ESM2 experiments and are reported in Table 3, along with the CMIP5 and CMIP6 multi-model mean values from Meehl et al. (2020). The model response to atmospheric CO₂ concentrations compares well with both CMIP multi-model ranges, especially for ECS that resulted to be well below the canonical 4.5°C threshold and is in line with estimates from the previous generation of models (see also Ch. 9 of IPCC, 2013).

A more straightforward measure of peak warming caused by anthropogenic CO₂ emissions is the transient climate response to emissions (TCRE), which is defined as the change in global mean near-surface air temperature per unit of cumulative CO₂ emissions at the time of CO₂ doubling (Gillett et al., 2013) and it applies to a similar timescale as the TCR. The TCRE was estimated here from the data of the 1pctCO₂ experiment following the methodology described in Arora et al. (2020), along with the associated cumulative CO₂ emissions (see Table 3). The climate response to emissions of CMCC-ESM2 is comparable to the ranges reported by Arora et al. (2020) for both CMIP5 and CMIP6 models, even if the diagnosed cumulative fossil fuel emissions are located at the low-end of the multi-model statistics. By breaking down the contribution of the carbon pool changes for atmosphere (595 PgC), ocean (231 PgC), and land (121 PgC), it emerges that the land component pool is rather small with respect to other CMIP models (see Figure A2 in Arora et al., 2020). However, such a response of the CLM 4.5 model lies within the range of the values simulated by the previous version of CESM1-BGC (62 PgC) and its latest implementation in CESM2 (248 PgC).

The linearized feedback framework for carbon cycles analyses described in Friedlingstein et al. (2006) was here applied to evaluate the strength of combined physical and biogeochemical global scale responses. Three metrics are thus considered: the linear transient climate sensitivity to CO₂ (α), the carbon-concentration feedback (β) to quantify the carbon cycle response to CO₂ changes as increase in oceanic and/or terrestrial carbon uptake per atmospheric CO₂ increase, and the carbon-climate feedback (γ) that measures the carbon cycle response to changes in physical climate as increase in oceanic and/or terrestrial carbon uptake per increase in global surface temperature.

These feedback parameters were computed following the C⁴MIP protocol (Jones et al., 2016) that recommends the use of data from two idealized fully coupled experiments, 1pctCO₂ and its biogeochemically coupled counterpart named 1pctCO₂-bgc, with values derived at the time of CO₂ doubling as suggested in Jones and Friedlingstein (2020). As reported in Table 3, the linear transient climate sensitivity to CO₂ is close to previous and current CMIP estimates, while the global carbon cycle response to changes in atmospheric CO₂ and surface temperature is slightly lower than the multi-model mean values. This provides a general indication on the reduced responsiveness of the model carbon cycle to changes in main system drivers, but comparing the individual contribution to carbon-concentration and carbon-climate feedbacks for land ($\beta_L = 0.49$ and $\gamma_L = -9.60$) and ocean ($\beta_O = 0.89$

and $\gamma_o = -11.16$) components with the values reported for CMIP6 by Jones and Friedlingstein (2020), the second component results to be much closer to other models than the first one. The low land carbon uptake of CLM4.5 relates primarily to a remarkable nitrogen limitation effect on the land vegetation growth that translates into reduced terrestrial carbon turnover and CO_2 exchange rate (see also Arora et al., 2020). According to the inter-comparison of different CLM version by Wieder et al. (2019), these limitations could be overstepped with the inclusion in the model of a flexible plant stoichiometry, energetic cost functions for carbon and nitrogen uptake, and a prognostic response of foliar photosynthetic capacity to environmental conditions.

3.2. Global Scale Climate Evolution in CMIP6 Experiments

In this section, an overview of selected metrics is presented to address relevant Earth System responses to anthropogenic and natural forcing simulated by CMCC-ESM2 under the historical climate conditions (1850–2014) and under future projections of ScenarioMIP up to year 2100 (see details in Table 1). Figure 1 illustrates the evolution of global mean annual values from the considered experiments, along with the global mean and one standard deviation interval obtained from the 500 years piControl simulation and the comparison with the pertaining time series from the most recent observational datasets.

Figure 1a represents the evolution of global warming with respect to the 1995–2014 average obtained from the near-surface air temperature fields, including the comparison with the temperature anomalies over the same period from the HadCRUT5 analysis data set (Morice et al., 2021).

In the historical period, the model shows a cooling trend up to 1900 and a consequent warming phase till the central decades of the twentieth century, when a cooling period temporarily counters the long-term warming trend, consistent with the phase sequence reported in Zhu et al. (2018). The most significant increase in global mean temperature occurs between 1975 and 2014 at a rate of 0.2°C per decade that is close to the HadCRUT5 data, namely 0.18°C per decade, and lower than the CMIP6 multi-model mean trend (0.24°C per decade in Papalexiou et al., 2020). However, the global warming signal simulated for the last decade of the historical experiment compared to the reference 1850–1990 average overestimates the temperature reconstruction of HadCRUT5, with mean values of 1.21°C and 0.95°C , respectively. The global temperature change simulated at the end of the 21st century for the different scenarios is in general agreement with CMIP6 multi-model mean values reported by Tebaldi et al. (2021), whereas results from ssp126 and ssp245 experiments are slightly above the respective ensemble means.

Figure 1b illustrates the global annual mean precipitation anomaly with respect to the 1995–2014 period, calculated as the sum of large scale and convective precipitation fields, in comparison to the GPCPv3.1 data available from year 1983 (Huffman et al., 2020). Precipitation anomaly evolves closely to the piControl interval for most of the historical period and it clearly departs from it in the middle of the twentieth century, coherently with the warming signal, although the model exhibits a positive mean bias of 0.27 mm d^{-1} in comparison to the observations over the reference period. Future projections indicate a steady increase of global precipitation throughout the whole 21st century, although ssp126, ssp245, and ssp370 simulations end with rather high, similar values and only the ssp585 scenario exhibits a marked change that compares well with CMIP6 multi-model estimates (Tebaldi et al., 2021).

Ocean heat content (OHC) anomaly within 0–2,000 m (Figure 1c) computed with respect to the 1950–2000 average from CMCC-ESM2 historical simulation compares satisfactorily with the observation-based reconstruction of Zanna et al. (2019). The OHC variation from 1871 to the end of the historical simulation corresponds to 693 ZJ that is exceeding the high-end value obtained from the reconstructed data set (436 ± 91 ZJ). It should be noted that the simulated OHC partly reflects the occurrence of volcanic eruptions, as shown in the inset plot for the major events of the twentieth century, namely Agung in 1963, El Chichon in 1982, and Pinatubo in 1991 (vertical dashed lines). This uneven response of the global mean OHC to specific eruptions is also affected by the background mean state of the system in correspondence of the event and by the contribution of the internal climate variability (see e.g., Fasullo et al., 2017; Predybaylo et al., 2020). Similarly to the near-surface temperature anomaly (Figure 1a), the OHC at the very beginning of the historical simulation is characterized by a slight departure from the long-term pre-industrial mean value. This discontinuity results from the combination of the residual negative drift of OHC in the piControl simulation (see Table S1 in Supporting Information S1) and from an artificial increase of temperatures due the transition from the mean state volcanic forcing used in piControl to

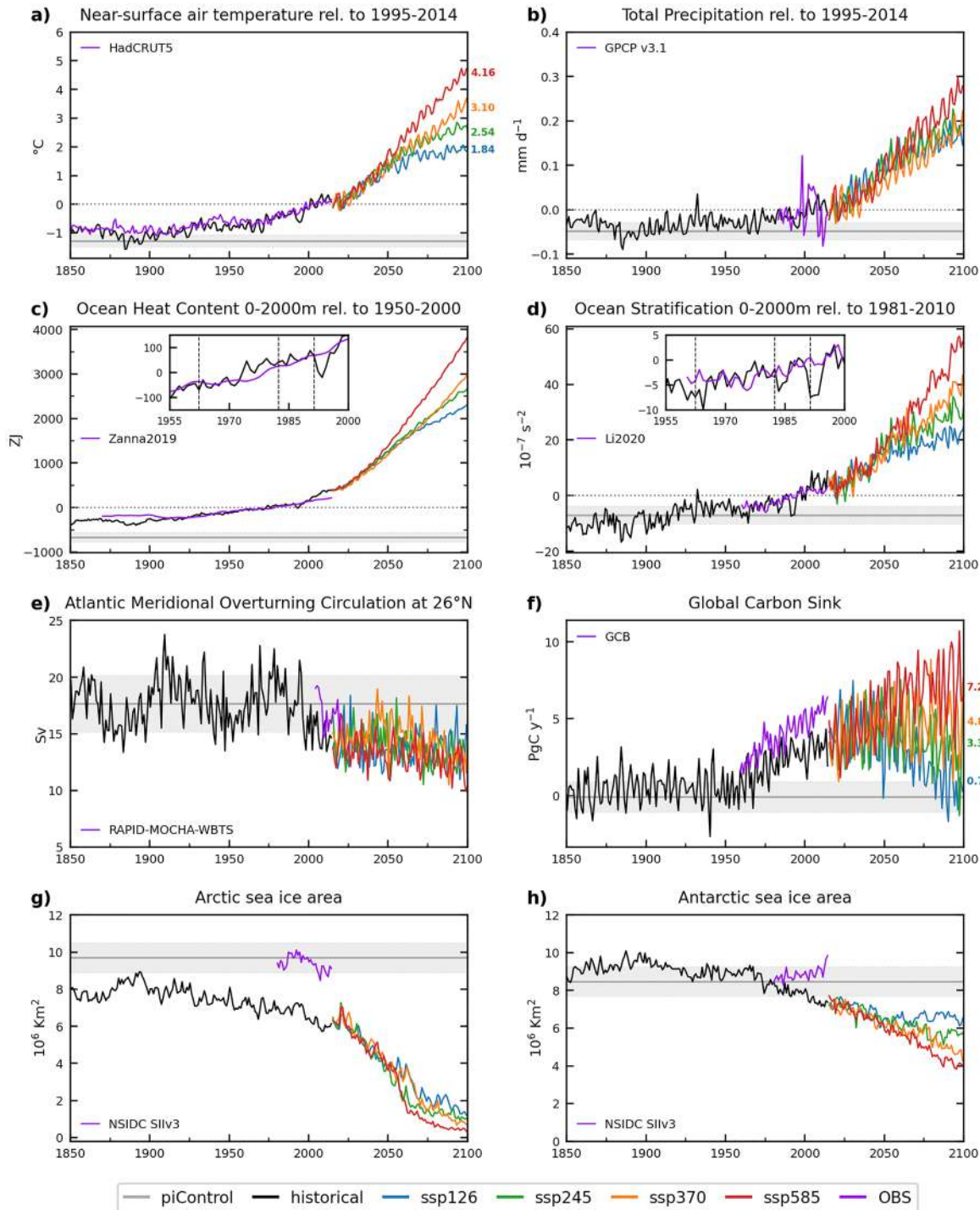


Figure 1. Time series of global mean annual values for selected climate metrics as monitored from available observational datasets (purple solid line) and as simulated by CMCC-ESM2 in historical (black solid line) and ScenarioMIP projections up to year 2100 (colored solid lines) for near-surface air temperature (a), total precipitation (b), 0–2,000 m ocean heat content (c) and stratification (d), Atlantic Meridional Overturning Circulation at 26°N (e), global land and ocean carbon sink (f), sea ice area in Arctic (g), and Antarctic (h) regions. *Note.* Global mean value (gray solid line) and one standard deviation interval (gray shaded area) obtained from the 500 years piControl simulation are also reported. Values reported on the right side of panels (a and f) refer to the mean value calculated over 2081–2100 for each scenario. Insets in panels (c and d) show historical and observations time series over the period 1955–2000, with vertical dashed lines representing the occurrence of major volcanic eruptions, namely Agung in 1963, El Chichon in 1982, and Pinatubo in 1991. In the carbon sink representation, a positive (negative) value indicates an uptake (release) of CO₂ from the combined land and ocean response.

the time-varying one of the historical experiment. The adjustment of temperatures occurred in the very beginning of the historical simulation determined a marked decrease of the sea ice distribution over the Arctic region (see Figure 1g).

The evolution of ocean stratification was addressed by considering the globally averaged square buoyancy frequency in the 0–2,000 m depth range relative to the 1981–2000 average (Figure 1d). This metric allows to better account for changes in the ocean vertical density structure that significantly impact the exchanges of heat, carbon, and biogeochemical quantities along the water column (Li et al., 2020). In agreement with the OHC evolution, simulated ocean stratification embeds the signature of large volcanic eruptions within the twentieth century (inset of Figure 1d). The cooling signal transferred to the ocean interior after each event is more evident than in OHC and it persists for few years before being damped out by the surface warming recovery. Recent estimates of ocean stratification based on the Institute of Atmospheric Physics temperature and salinity data set reported by Li et al. (2020) indicate a robust upward trend of $1.5 \times 10^{-8} \text{ s}^{-2}$ per year between 1960 and 2018, which corresponds to a 5% change with respect to the reference time window. In the historical experiment, the model produces a rather similar trend ($2.2 \times 10^{-8} \text{ s}^{-2}$ per year) and change (4.1%) over the period 1960–2014, but values are expected to be far larger in the future projection with global mean changes up to 27.9% by the end of 2100 in the ssp585 scenario.

Figure 1e represents the evolution of the Atlantic Meridional Overturning Circulation (AMOC) at 26°N derived from simulated data as the annual mean of monthly meridional transport maximum value over depth and observed by the RAPID-MOCHA-WBTS array (Frajka-Williams et al., 2020) for the period 2004–2020. In the historical experiment, AMOC variability is characterized by a marked oscillation of about 50 years that determines a negative trend in correspondence of the observational time window, with an average difference between model data and observations of -2.11 Sv . Projected changes of the AMOC in 2081–2100 relative to present day (2005–2014) points toward a reduction that ranges from a minimum of -4.7% in ssp126 up to -17.8% for the ssp585 scenario. These values are in general agreement with the estimates based on the CMIP5 multi-model ensemble for RCP2.6 ($-11 \pm 14\%$) and RCP8.5 ($-32 \pm 14\%$) from the IPCC Special Report on the Ocean and Cryosphere report (SROCC; IPCC, 2019), but below the projected reduction range of 34%–45% obtained by Weijer et al. (2020) using CMIP6 data.

The global carbon sink due to the cumulative response of land and ocean components to rising CO_2 concentrations, temperature and land cover changes (Figure 1f) was compared over the historical period with the reconstruction provided by the Global Carbon Budget 2020 data set (GCB; Friedlingstein et al., 2020). Over the period 1959–2014 the simulated data present an average difference with GCB estimates of -1.69 PgC y^{-1} as a direct consequence of the rather low carbon turnover of the land component (see also Section 3.1). Beside this bias, the model reproduces coherently the interannual variability of 1.16 PgC y^{-1} ($\text{GCB} = 1.32 \text{ PgC y}^{-1}$) and to a lower extent the decadal trend of 0.45 PgC y^{-1} ($\text{GCB} = 0.73 \text{ PgC y}^{-1}$). The comparison of the simulated carbon sink evolution in 2081–2100 relative to 2005–2014 under the different future climate scenarios highlights a decrease toward pre-industrial values by year 2100 for the ssp126 experiment (0.77 PgC y^{-1}), while larger values occur in the other scenarios according to the increased anthropogenic forcing prescribed.

Figures 1g and 1h provide a closer view of the yearly averaged marine sea ice area in the Arctic and Antarctic regions, respectively, under historical conditions and CMIP6 future projections. The observational data set is the Sea Ice Index version 3 (SIIv3; Fetterer et al., 2017) produced by the National Snow and Ice Data Center that relies on a composite analysis of remotely acquired images of sea ice between 1979 and 2014. Over the recent decades, the model remarkably underestimates the observed sea ice area in both Arctic and Antarctic regions being the differences with SIIv3 equal to -2.9×10^6 and $-1.1 \times 10^6 \text{ Km}^2$, respectively. In particular, the sea ice area over the Arctic region is far below the long-term mean of the piControl simulation since the beginning of the historical experiment. As previously noted, the transition in the volcanic forcing conditions determined an initial adjustment of temperatures with a sudden reduction of sea ice coverage in the northern hemisphere. Future projections over the Arctic region are close to each other with annual mean values below $2.0 \times 10^6 \text{ Km}^2$ by the year 2100. Conversely, Antarctic sea ice area in the historical period is rather steady and it coherently decreases from the mid of the twentieth century. The projected evolution of sea ice area for this region is characterized by a larger spread of the considered scenarios, with mean values between 6.6 and $4.2 \times 10^6 \text{ Km}^2$ over the period 2081–2100.

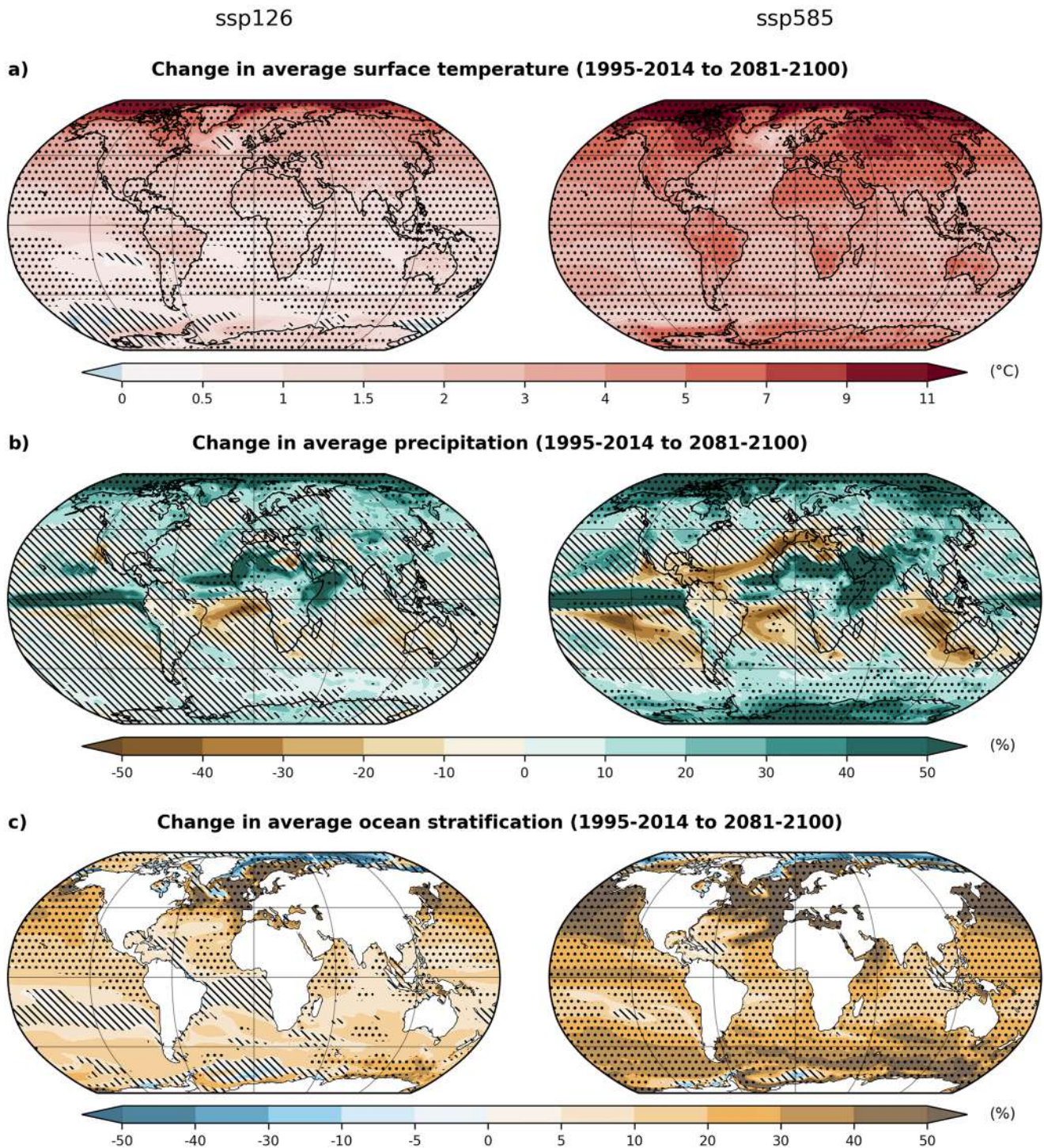


Figure 2. Changes in annual mean surface temperature (a), precipitation (b), and ocean stratification (c) based on CMCC-ESM2 projections for 2081–2100 relative to 1995–2014 under the ssp126 (left) and ssp585 (right) scenarios. The internal variability of the system was computed from the 500 year-long piControl experiment and stippling indicates areas where simulated changes are larger than 2 standard deviations, while hatching represents changes below 1 standard deviation.

Figure 2 shows the spatial distribution of simulated surface air temperature, precipitation, and ocean stratification changes until the end of the 21st century according to the lowest ssp126 and strongest ssp585 emission scenarios. Note that hatch pattern overlays are used to represent values below one (lines) or above two (points) standard deviations computed from the 500 years control simulation.

Table 4

Summary of Key Land Carbon and Nitrogen Fluxes and Pools as Obtained From CMCC-ESM2 Historical Simulation Between 1995 and 2014 and Observation-Based Estimates and CMIP6 Land-Only Spread

	Autotrophic respiration (PgC y ⁻¹)	Heterotrophic respiration (PgC y ⁻¹)	Gross primary production (PgC y ⁻¹)	Biological nitrogen fixation (TgN y ⁻¹)	Vegetation carbon (PgC)	Vegetation nitrogen (PgN)	Soil and litter carbon (PgC)	Soil and litter nitrogen (PgN)
Observation	45–50 ^b	57–73 ^c	113–125 ^d	52–141 ^e 40–100 ^f	343–539 ^g		1,837–3,257 ^g 2,157–2,293 ^h	133–140 ^h
CMCC-ESM2	62	42	108	96	423	3.1	2,917	262
CMIP6 land-only ^a	57–82	44–53	115–142	46–107	349–579	1.8–3.6	682–3,249	38–291

^aDavies-Barnard et al. (2020). ^bAutotrophic respiration: Piao et al. (2010) and Luysaert et al. (2007), present-day estimate for forests from 2007. ^cHeterotrophic respiration: Bond-Lamberty and Thomson (2010), soil respiration estimate for 2008. To account for the included root respiration, we reduced the literature estimate by 33% according to Bowden et al. (1993). ^dGross primary production: Jung et al. (2011), averaged estimate for 1982–2011. ^eBiological nitrogen fixation: Davies-Barnard and Friedlingstein (2020), upscaled averages for 1980–2019. ^fBiological nitrogen fixation: Vitousek et al. (2013). ^gSOM + Litter and Vegetation C: Carvalhais et al. (2014), present-day estimate for 2014. ^hSoil nitrogen in the top 1 m and soil carbon in the top 1 m (Batjes, 2014).

Temperature changes exceed the two standard deviations of piControl interannual variability over the polar regions in both scenarios (Figure 2a) and higher values extensively spread over the entire northern hemisphere in the ssp585 scenario. In particular, temperatures are projected to increase by about 7°C over the Canadian and Siberian areas and by 11°C in the whole Arctic region. The most relevant change between the two scenarios occur in the Southern Ocean, where values being below one standard deviation of piControl variability in the ssp126 scenario undergo a robust increase in the strongest emission forcing. The temperature response produced by CMCC-ESM2 reflects the spatial pattern and magnitude of results from the multi-model CMIP5 ensemble projections reported in the IPCC AR5 Synthesis Report (IPCC, 2014).

Overall differences in the projected changes of precipitation between the two scenarios are less pronounced (Figure 2b), whereas the polar regions as well as the African and Pacific equatorial areas show prominent variations. Even if changes in the simulated precipitation patterns do not exhibit clear variation trends as for the temperature, it is worth to note that all extratropical regions in the ssp585 scenario are affected by a reduction between 20% and 30% that is nearly above one standard deviation of the control simulation. Moreover, future changes in the Arctic and equatorial precipitations above the 40% threshold obtained under ssp126 forcing conditions further amplify under the strongest scenario with relevant increases over the entire Southern Ocean.

Future ocean stratification changes (Figure 2c) simulated in the ssp126 experiment are more pronounced along the oceanic temperate band of the northern hemisphere, while the expected variability in the southern hemisphere is largely below the one standard deviation threshold. A more robust increase of ocean stratification is expected instead under the ssp585 scenario, being differences well above the 25% of reference climate state and values nearly over the whole globe above the two standard deviations of the control simulation. It is worth to note that the reduction of sea ice formation throughout the year in the polar regions leads to a general decrease of the stratification, with changes up to –40% in the Arctic area.

3.3. Land Biogeochemical Cycles

The ability of CMCC-ESM2 to reproduce the carbon and nitrogen cycles on land is evaluated against observation-based estimates from the literature and available observational data products. In particular, recent literature estimates are used for the assessment of the simulated carbon and nitrogen pools and fluxes over the 1995–2014 period (Table 4).

The ecosystem respiration, here partitioned between its autotrophic and heterotrophic components, is characterized by an overestimation of the autotrophic term and an underestimation of the heterotrophic one, which was found to be a rather common bias in CMIP6 land biogeochemical models (see Davies-Barnard et al., 2020). The average gross primary production (GPP) simulated under present climate conditions is slightly below the lower bound of the estimates from Jung et al. (2011). Nitrogen inputs generated through the BNF process fall well within the observational range. However, the present-day value of BNF is close to the upper bound of the observed range (see Davies-Barnard & Friedlingstein, 2020), which is likely determined by the adopted empirical

relation between BNF and net primary production (see Section 2.1.2). In fact, other CMIP6 land biogeochemical models using a similar empirical parameterization were found to obtain a comparably high BNF values (Davies-Barnard et al., 2020). The carbon and nitrogen pools under present climate conditions are overestimated in CMCC-ESM2. In particular, the soil nitrogen pool nearly doubles the observed values, while the simulated soil carbon pool overestimation is less sizable. On the other hand, the carbon stock is two times larger than the estimate from the CMIP6 multi-model mean (Ito et al., 2020). Similarly, the model produces high values of vegetation carbon and nitrogen pools, with the former being close to the upper bound of the literature's estimated range. Despite a large amount of carbon and nitrogen in the vegetation and soil pools, fluxes are in good agreement with observed data (Table 4).

Overall, CMCC-ESM2 simulated fields in the present climate lie in the upper range or slightly above the observed values, with the exception of heterotrophic respiration that is underestimated, while results are mainly located in the higher portion of the CMIP6 multi-model spread.

In Figure 3, the spatial distribution of GPP, Leaf Area Index (LAI) and phenology (start and end of the vegetation growing season, respectively GSS and GSE) as reproduced by CMCC-ESM2 are evaluated against remotely acquired data over the period 2000–2014 to match the temporal extension of available observations.

The model overestimates GPP compared to observations from the FluxSat version 2 data set (Joiner & Yoshida, 2021) and large differences occur over northern Canada, Alaska, and in localized equatorial areas. This surplus of production is less dramatic over the Congo basin, the Maritime Continent, and southeast China, where absolute values are higher (Figure 3b). Conversely, CMCC-ESM2 underestimates GPP in many tropical regions, such as in the east and southeast Brazil, the Sahel, and the sub-tropical Southern Africa, where the mismatch exceeds by 50% the observed values. Relatively lower negative biases are present in the northern midlatitudes and in the Southeast Asia. Despite these biases, the latitudinal distribution pattern of GPP is accurately represented by CMCC-ESM2 (Figure 3c).

A similar spatial pattern of biases is visible in the simulated LAI when compared to the MODIS version 6 satellite-based observation (Myneni et al., 2015a, 2015b). A notable exception is the LAI overestimation in the intensely farmed northern mid-latitudes, that contrasts with the generally negative GPP bias. This mismatch could be due to the rather simple representation of crop fields in CLM4.5, but a few authors recently suggested possible inconsistencies in the LAI satellite datasets, that can cause uncertainties in the derived GPP estimates (Xie et al., 2019). Simulated LAI overestimation is more pronounced in eastern China, eastern US, and most of all in the northern high-latitudes, where the index is increased more than twofold compared to observations (Figure 3e). Underestimations are limited to the subtropical regions, as for GPP. The LAI latitudinal distribution reflects these characteristics, and turns out to be generally larger than MODIS in most latitudinal bands (Figure 3f).

The LAI portrays the projected area of leaves over a unit of land (Waring & Running, 2010) thus representing a proxy for plant phenology at the seasonal and interannual time-scales. In this context, the Four Growing Season Type method based on LAI (Peano et al., 2019) allows a sound estimation of start and end of the vegetation growing season. CMCC-ESM2 correctly simulates the GSS in the midlatitudes (Figure 3h), while GSE is well represented in the north hemisphere high-latitude (Figure 3k). The latitudinal distribution of GSS and GSE highlights a 2-month delay in GSS timings in the north hemisphere high-latitude (Figure 3i) and about 2-month GSE timings in advance in the north hemisphere tropics (Figure 3l). These results are similar to those obtained from a selection of seven CMIP6 land biogeochemical models as reported by Peano et al. (2021). In particular, the simulation of vegetation onset and offset is more problematic in the southern hemisphere, where growing season is generally longer in the CLM4.5 model (namely with an earlier start and later end of the growing season). This bias is throughout discussed in Peano et al. (2019).

The annual mean evolution of GPP (Figure 4a) and BNF (Figure 4b) over the historical and future scenarios are characterized by a slight increasing trend from the pre-industrial period until the year 1920. The average values equal to 93 PgC y⁻¹ and 89 TgN y⁻¹, respectively, with BNF characterized by a much larger interannual variability. Afterward, both GPP and BNF show a continuous increase during the 20th and 21st centuries that closely reflects the global mean warming signal (see Figure 1a). The ssp126 scenario reaches a new quasi-steady-state condition by the end of the current century, with GPP and BNF mean values over the period 2081–2100 increased by 36% (125 PgC y⁻¹) and 15% (102 TgN y⁻¹) with respect to the pre-industrial ones. Oppositely, the ssp585

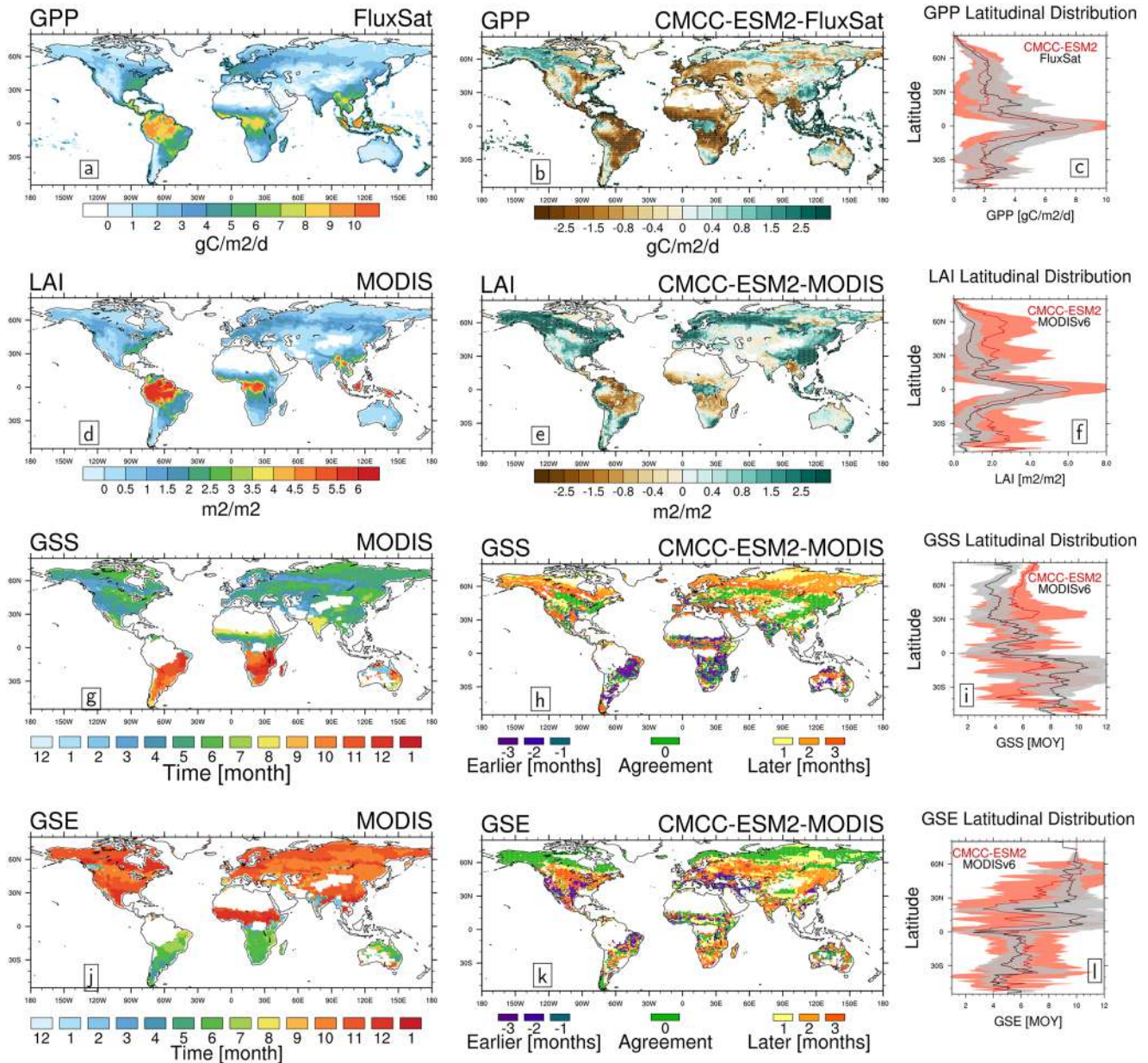


Figure 3. Comparison of CMCC-ESM2 historical data averaged between 2000 and 2014 against observational datasets for (a) gross primary production (GPP) from FluxSat version 2 (Joiner & Yoshida, 2021), (d) Leaf Area Index (LAI) from MODIS version 6 (Myneni et al., 2015a, 2015b), (g) start and (j) end of the Growing Season (GSS and GSE, respectively) derived from MODIS LAI data through the Four Growing Season Type (4GST) method by Peano et al. (2019). Spatial maps show the difference between observed and simulated (b) GPP; (e) LAI; (h) GSS; and (k) GSE. The last columns show the latitudinal distribution of observed and simulated (c) GPP; (f) LAI; (i) GSS; and (l) GSE, and the shading represents one standard deviation. *Note.* The panels cover the latitudinal range between 55°S and 80°N.

scenario GPP (BNF) mean value increases by 60% (23%) above pre-industrial one at the end of the 21st century and it is expected to go far above (Figures 4a and 4b).

The evolution of global mean carbon and nitrogen of aggregated soil and litter pools (Figures 4c and 4d) are largely influenced by the land-use pathways, showing an initial decrease during the early part of the historical simulation that is followed by a stable period up to the first decades of the twentieth century and a marked, constant increase after the 1950s in agreement with findings from Ito et al. (2020). In all future scenarios both carbon and nitrogen aggregated pools are characterized by an increase up to 2100, with extremes values reached by the ssp126 and ssp370 scenarios, which are respectively distinguished by maximum afforestation and deforestation interventions (O'Neill et al., 2016). Similar historical and scenario trajectories have been reported for other

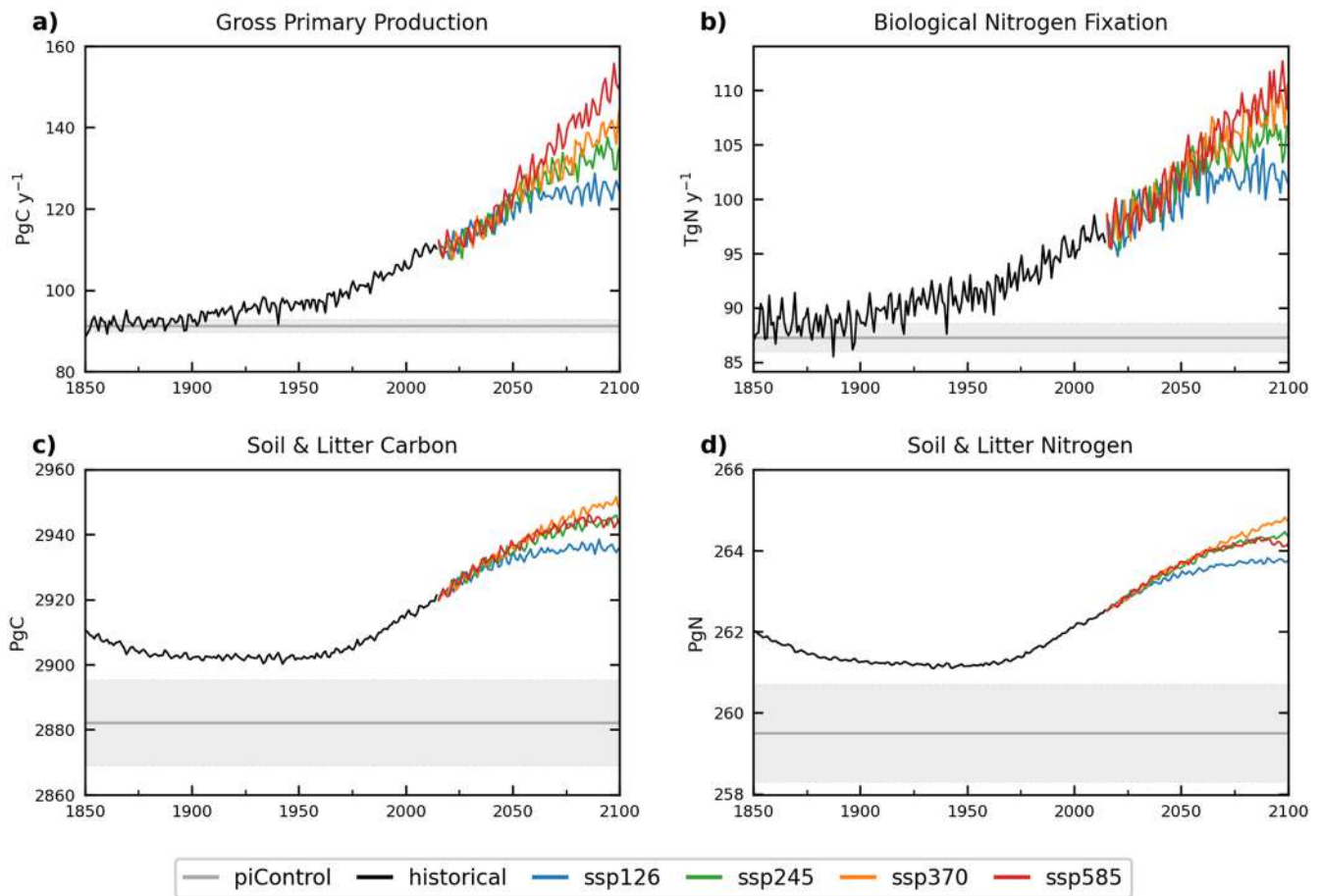


Figure 4. Time series of global annual mean values simulated by land component of CMCC-ESM2 in historical (black solid line) and ScenarioMIP projections up to year 2100 (colored solid lines) for gross primary production (a), biological nitrogen fixation (b), soil plus litter carbon (c), and nitrogen (d) content. *Note.* Global mean value (gray solid line) and one standard deviation interval (gray shaded area) obtained from the 500 years piControl simulation are also reported.

models in a set of CMIP6 simulations analyzed by Ito et al. (2020). However, the projected changes in carbon and nitrogen aggregated soil and litter pools during the 21st century scenarios have a magnitude close to the difference between historical and pre-industrial simulations. This discrepancy arises from the negative drift of the piControl simulation (see Table S1 in Supporting Information S1) and poses clear limitations to the level of confidence in the projected changes.

3.4. Ocean Biogeochemistry Evaluation

Model performance in relation to ocean biogeochemical cycles is firstly addressed by considering the spatial distribution of major biogeochemical properties in the upper ocean and across the water column as reproduced in CMCC-ESM2 historical simulation between 1995 and 2014 and the available observational data products (Figure 5).

The upper ocean chlorophyll-a concentrations obtained from the satellite derived ESACCI-OC v3.1 (Sathyendranath et al., 2018) data over the period 2000–2014 compares rather satisfactorily with model outcomes (Figure 5a). CMCC-ESM2 data were vertically averaged over the optical depth calculated following the approach of Vichi et al. (2007). Negative biases occurring in several coastal regions of the northern hemisphere are likely due to the lack in the representation of land born nutrients input. The model has also few skills in reproducing the chlorophyll-a patterns along the Eastern Boundary Upwelling Systems, where the representation of the seawater physical properties is particularly limited by the underlying coarse resolution of the model (see e.g., Figure S1 in Supporting Information S1). Meanwhile, the lower concentrations occurring in the subtropical gyres are

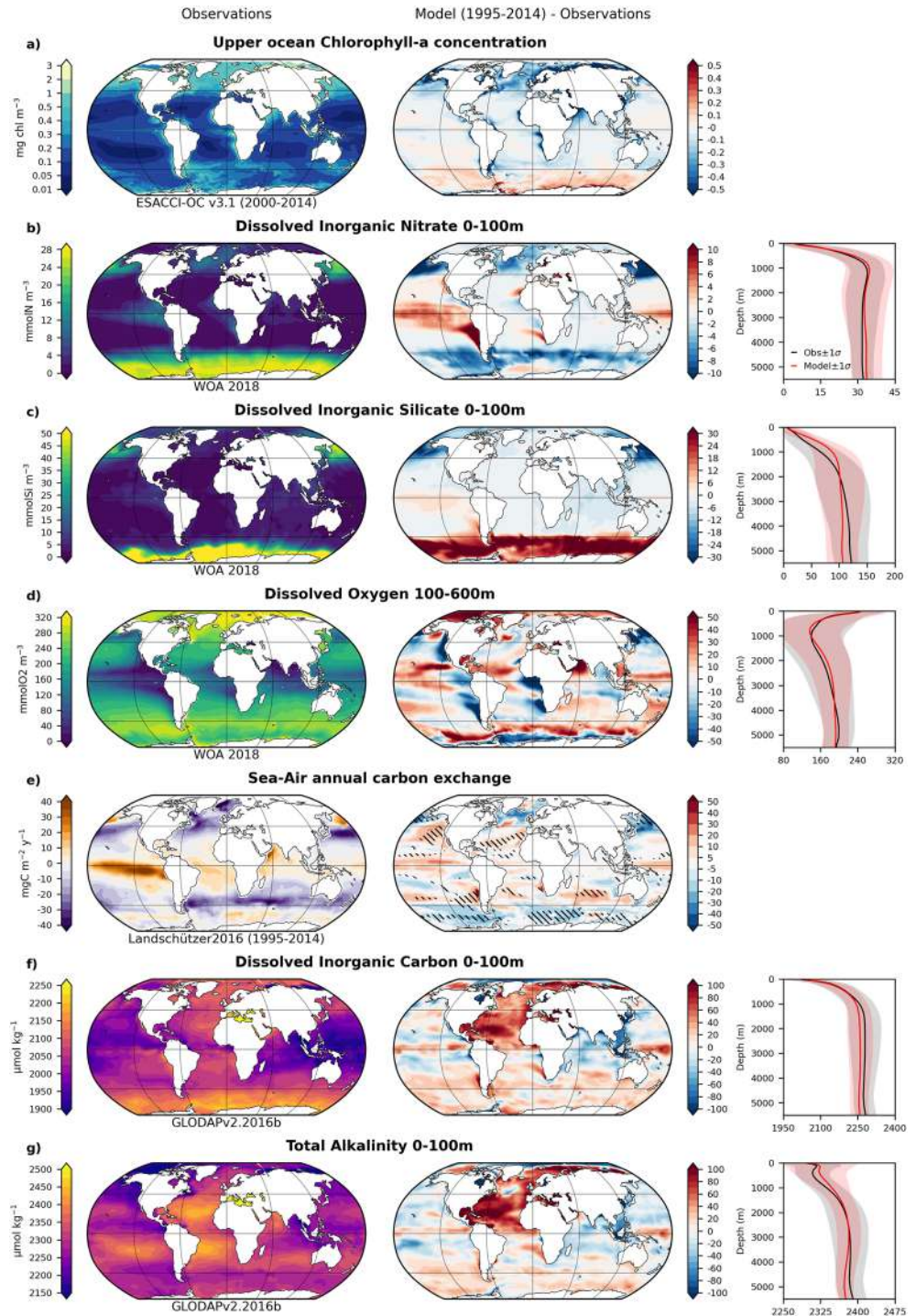


Figure 5. Comparison of CMCC-ESM2 historical data averaged between 1995 and 2014 against different observational datasets for upper ocean Chlorophyll-a concentrations (a), 0–100 m concentrations of dissolved inorganic nitrogen (b) and silica (c), dissolved oxygen concentration between 100 and 600 m (d), sea-air carbon dioxide exchanges (e), 0–100 m concentrations of dissolved inorganic carbon (f), and total alkalinity (g). Spatial maps show observed upper ocean fields on the left and model-to-data differences in the central panels, while the right ones illustrate the vertical distributions of global annual mean and standard deviations values from simulated (red) and observed (black) fields. Simulated upper ocean chlorophyll-a concentrations were vertically averaged over the optical depth as in Vichi et al. (2007). The sea-air carbon exchange differences (e, right panel) are positive (negative) in the case of a release (uptake) of CO₂ from the atmosphere and hatched regions indicate where model and observations fluxes have opposite signs.

adequately simulated, whereas it must be noted that the bias range ($\pm 0.05 \text{ mg Chl m}^{-3}$) is rather close to the typical values of the observations. Chlorophyll-a concentrations are systematically overestimated throughout the year over the circumpolar Antarctic region, where the simulated mixed layer depth is far too deep (see Figure S1c in Supporting Information S1) and leads to an increased upwelling of nutrients (especially silicate) that sustains the predominant diatom's functional group. As shown in Figure S2 in Supporting Information S1, this overestimation over the Southern Ocean is sustained also by the slightly higher dissolved iron concentrations simulated by the model with respect to the ocean surface data from GEOTRACES observations (GEOTRACES IDP, 2021).

The comparison of simulated dissolved inorganic nitrate (Figure 5b) and silicate (Figure 5c) concentrations against World Ocean Atlas 2018 (WOA; Garcia et al., 2018a) annual mean values over the 0–100 m layer show a distinct pattern that relates to the chlorophyll-a bias over the Antarctic ocean: nitrate is over consumed on the rim of the circumpolar current by phytoplankton whose growth is mainly sustained by the high dissolved silicate concentrations. However, spatial distributions of nitrate and silicate are in general agreement with observations, reflecting the high-nutrient low-chlorophyll regime of the eastern equatorial Pacific Ocean and with minor deviations along the coastal areas. A major negative bias with respect to the observed data emerges in the North Pacific Ocean where nutrients values are underestimated, not dissimilarly from other CMIP6 models (see e.g., Séférian et al., 2020). The global averaged vertical profiles for both nutrients agree well with WOA data and the spatial variability over the different depths is characterized by comparable variability.

Dissolved oxygen concentrations from CMCC-ESM2 historical simulation and WOA 2018 (Garcia et al., 2018b) data averaged in the 100–600 m depth range are compared in Figure 5d. This interval was adopted to align with the potential expansion horizon for oxygen minimum zones identified in the recent SROCC IPCC report (IPCC, 2019). Differences in open ocean areas are contained within $\pm 10 \text{ mmol m}^{-3}$ and most relevant deviations occur in the tropical oxygen minimum zones and the Southern Ocean. In particular, the simulated pattern of tropical oxygen minima has a rather weak extension toward the open ocean and a marked dipole bias overlapping the Antarctic circumpolar region. Nevertheless, the simulated global mean vertical profile and standard deviations for oxygen concentrations compare well to those from WOA, with slightly lower values between 500 and 1,000 m.

Figure 5e shows the simulated annual mean sea-air CO_2 exchange in comparison with the observational data interpolations of Landschützer et al. (2016) over the same time period. Differences are overall contained between $\pm 5 \text{ mgC m}^{-2} \text{ y}^{-1}$ and marked deviations from the observational data set are visible in oceanic regions characterized by prominent circulation features, such as the western boundary currents, Antarctic circumpolar current, and the Pacific equatorial upwelling. It is here important to distinguish between lacking processes of the model: the physical representation of boundary currents is still limited by the coarse horizontal model resolution (see e.g., Tsujino et al., 2020), which negatively affects the ecosystem driven CO_2 fluxes off the coastal areas, while the intense primary production in the Southern Ocean generates an ingassing of CO_2 that persists all round the year. The generated organic matter stimulates the growth of heterotrophic bacteria that further contribute through the remineralization to replenish the inorganic nutrient pools. Conversely, the rather low phytoplankton concentrations in the northeastern Pacific and northern tropical Atlantic regions determines CO_2 exchanges opposite to the observed ones.

The model correctly reproduces the annual mean spatial patterns of observed DIC (Figure 5f) and TA (Figure 5g) provided by the observational gridded data set GLODAPv2 (Lauvset et al., 2016). Differences across the oceanic basins are well below $20 \text{ } \mu\text{mol kg}^{-1}$, with the exception of the North Atlantic Ocean where a positive bias emerges for both DIC and TA. In this region, TA overestimation occurs predominantly within the subtropical gyre in response to a shift of the evaporation-precipitation balance, which is also reflected in the positive bias of seawater surface salinity (Figure S1b in Supporting Information S1). Thus, the higher seawater buffering capacity leads to a stronger uptake of atmospheric CO_2 with an increase of DIC concentrations. The vertical distribution and variability for both variables is coherent with GLODAPv2 data, whereas DIC mean values below 1,000 m are systematically lower than present time conditions by about $10 \text{ } \mu\text{mol kg}^{-1}$. This offset relates to the weak CO_2 penetration from the upper ocean toward the interior and it is attributable to a limited representation of key physical processes in low horizontal resolution models, such as deep ocean ventilation and circulation.

Table 5 summarizes the global scale response under current climate conditions of CMCC-ESM2 for a set of surface and inner ocean variables central to carbon and nutrient cycling, including observational estimates and CMIP multi-model statistics. The model provides a reliable representation of the sea surface pH trend in the

Table 5

Comparison of Key Global Oceanic Biogeochemical Quantities Computed From CMCC-ESM2 Historical Simulation Between 1995 and 2014 With Estimates of Current Climate Conditions for Observational Data Minimum/Maximum Range and From CMIP5 and CMIP6 Multi-Model Mean and Standard Deviations Statistics

	Surface net carbon uptake (PgC y ⁻¹)	Surface pH trend (units decade ⁻¹)	Net primary production (PgC y ⁻¹)	Particulate carbon export at 100 m (PgC y ⁻¹)	Calcite export at 100 m (PgC y ⁻¹)
OBS range	2.1/2.3	-0.014/-0.022	38.8/52.1	5.8/12.9	0.38/1.64
CMCC-ESM2	1.9	-0.017	29.7	5.7	0.41
CMIP5	2.1 ± 0.4 (12)	-0.012 ± 0.004 (10)	39.8 ± 18.9 (11)	7.2 ± 2.3 (11)	0.48 ± 0.23 (11)
CMIP6	2.2 ± 0.2 (14)	-0.016 ± 0.0003 (13)	38.9 ± 12.3 (13)	7.5 ± 1.9 (13)	0.60 ± 0.24 (13)

Note. Observation ranges were obtained from S  ferian et al. (2020), with the exception of surface pH trend from Lauvset et al. (2016). CMIP6 data for surface pH trend are from Kwiatkowski et al. (2020), as the list of CMIP5 models here used to compute the related multi-model statistics. CMIP multi-model statistics for all other variables were derived from S  ferian et al. (2020). Values within parentheses indicate the number of considered models.

period 1995–2014 compared to both the recent CMIP6 multi-model ensemble and the estimates from the data reconstruction of Lauvset et al. (2016). Carbon uptake from the atmosphere is slightly below the observational range, whereas still within the spread of different CMIP multi-model ensembles. This relates to the far underestimated simulated primary production (29.7 PgC y⁻¹) compared to the observational range (38.8/52.1 PgC y⁻¹) and it is also conditioned by the previously described biases in the CO₂ exchanges occurring, for example, within the Southern Ocean and northern tropical Atlantic area (see Figure 5e). As reported by S  ferian et al. (2020), several CMIP6 models are outside the observational primary production ranges thus pointing to the need of better constraining remote-sensing-based estimates. Although the simulated primary production is still within CMIP5 and CMIP6 multi-model variability, a lack in the carbon transfer toward organic matter pools emerges also in the vertical export of particulate organic carbon and calcite, with mean values close to the lower limit of observation intervals. In general, the weak primary production directly reflects on the stock of organic matter and it could be associated to an uneven balance in the model of respiration and organic matter losses, which control the outgoing carbon pathways from phytoplankton.

In line with the recent assessment of marine drivers of the IPCC SROCC report (IPCC, 2019), the analysis of CMCC-ESM2 responses simulated under future climate projections of ScenarioMIP experiments focused on changes occurring in surface pH, subsurface dissolved oxygen concentrations (100–600 m), upper ocean dissolved nitrate concentration (0–100 m), and net primary production (Figure 6).

The simulated reduction in the global ocean surface pH during the historical period corresponds to ~0.1 units and it is projected to intensify throughout the 21st century in most of the scenarios, with the exception of ssp126 showing a moderate decrease after 2060 (Figure 6a). Since the pre-industrial period, the global decline in surface pH obtained in each simulated scenario is remarkably close to the CMIP6 multi-model mean values reported by Kwiatkowski et al. (2020). A clear reduction of subsurface dissolved oxygen concentration characterizes the entire simulated period, with changes varying between -3.7% and 7.4% over 2081–2100 with respect to current climate conditions (Figure 6b). Similar values are reported also in IPCC SROCC report (IPCC) for CMIP5 scenarios, whereas the extent of such changes is still debated due to evidences showing a relation of interannual climate variability with oxygen minimum zones extension over past decades (Deutsch et al., 2011; Duteil et al., 2018) and the limited skills of marine models with coarse horizontal resolution in reproducing ventilation and mesoscale mixing processes (Busecke et al., 2019; L  vy et al., 2021).

The evolution of net primary production (Figure 6c) is characterized by a relative increase at the beginning of historical simulation, with a larger contribution from the phytoplanktonic activity within the tropical zone (Figure S3c in Supporting Information S1). At these latitudes, the previously remarked transition in the volcanic forcing conditions (see Section 3.2) lead to an initial increase of temperatures and light availability that stimulates the growth of phytoplankton. The cooling phase lasting up to 1900 damps this initial spike and afterward the trend remains rather stable up to 2050, when it increases to a different extent in all scenarios, namely between 2.6% and 6.4% by the end of 2100. Although this might appear in disagreement with the negative tendency of both CMIP5 and CMIP6 multi-model means (see Fr  licher et al., 2016; Kwiatkowski et al., 2020), it is worth noting

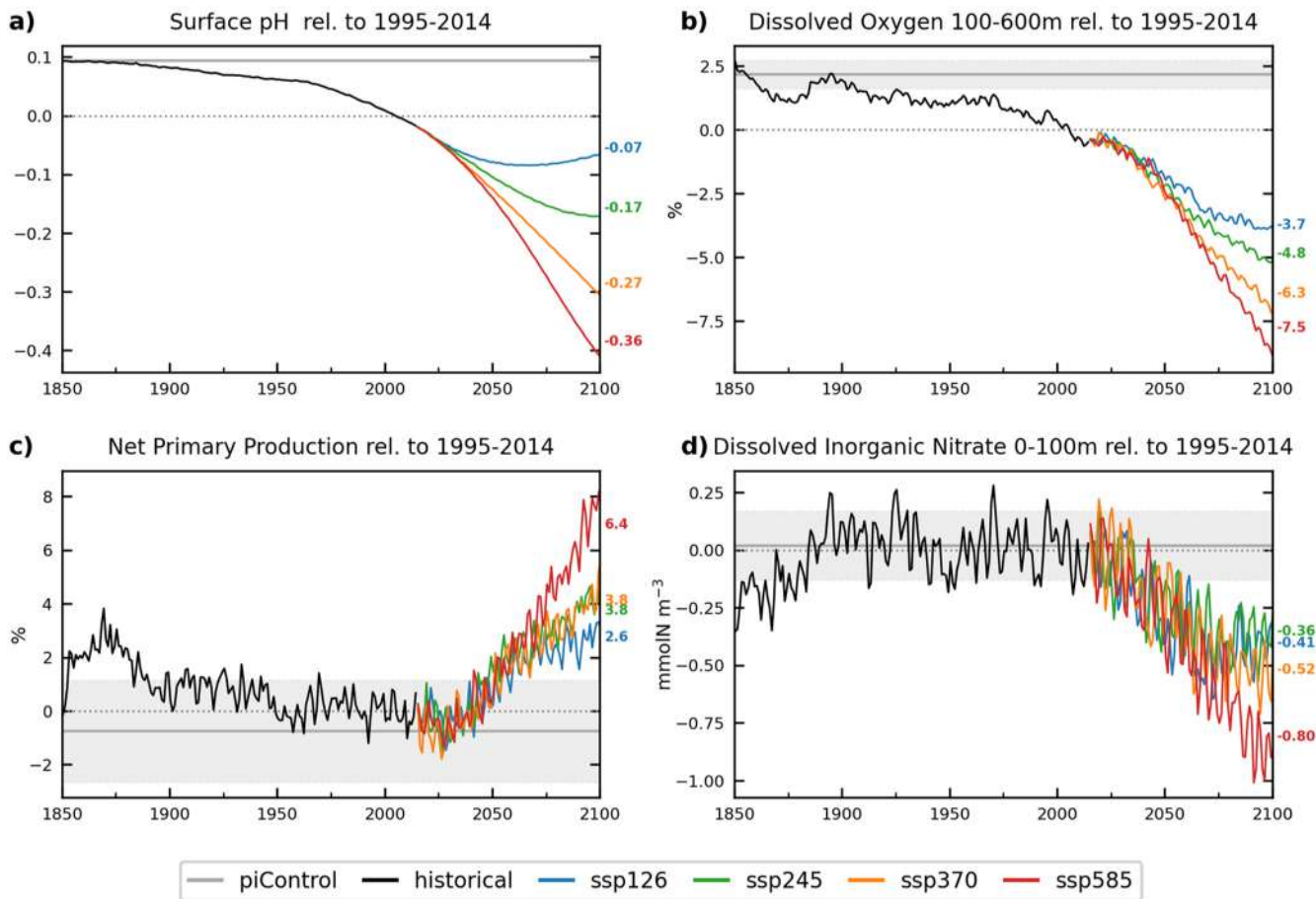


Figure 6. Time series of global annual mean values for surface pH (a), dissolved oxygen concentrations between 100 and 600 m (b), net primary production (c), and dissolved inorganic nitrate concentrations between 0 and 100 m (d) as simulated by CMCC-ESM2 in historical (black solid line) and ScenarioMIP projections up to year 2100 (colored solid lines). Values reported on the right side of panels refer to the average calculated over 2081–2100 for each scenario relative to 1995–2014. Dissolved oxygen and net primary production are shown as the percentage change with respect to the 1995–2014 average value. *Note.* Global mean value (gray solid line) and one standard deviation interval (gray shaded area) obtained from the 500 years piControl simulation are also reported.

that the uncertainty expressed by the inter-model standard deviation is very large, in some cases up to five times the mean value. It clearly emerges that global mean primary production, its spatial patterns and its temporal evolution under historical conditions and future climate scenarios is still significantly uncertain (Tagliabue et al., 2021). This is due to the complex interplay between physical drivers, ecosystem interactions, and physiological response of organisms in the lower trophic levels and poorly constrained by scarce observational data and diverging remote-sensing based approaches (Sathyendranath et al., 2020).

Figure 6d shows that the simulated evolution of dissolved nitrogen concentrations has similar variability ranges between historical and piControl simulations up to year 2025, when scenario projections start to diverge with a decline of upper ocean values ranging from -0.36 to -0.80 mmolN m^{-3} in ssp126 and ssp585, respectively. Such a decline in future dissolved nitrogen concentrations from surface waters is in good agreement with results from CMIP5 and CMIP6 projections (Kwiatkowski et al., 2020). Despite the potential limitations related to the oceanic model resolution, this result directly supports the reliability of the simulated ocean stratification that primarily controls the trapping of inorganic nutrients in the ocean interior (Moore et al., 2018).

4. Summary and Conclusions

This work introduces the second generation CMCC-ESM2, along with its application to a set of key coupled climate-carbon experiments as a contribution to sustain the CMIP6 initiative. The physical core of the model is based on its climate counterpart (CMCC-CM2-SR5) and a number of new features were specifically addressed

to extend the representation of both marine and terrestrial biogeochemical processes with respect to its CMIP5 predecessor. In particular, land biogeochemistry was extended to a wider set of carbon pools and PFTs, along with a prognostic representation of the nitrogen cycle. The marine ecosystem representation was reshaped toward an intermediate complexity of lower trophic level interactions but including a dynamic benthic compartment and a new formulation of heterotrophic bacterial population.

Climate sensitivity metrics evaluated from the analysis of CMCC-ESM2 coupled experiments are close to the multi-model mean values of both CMIP5 and CMIP6 ensembles, while the climate–carbon cycle feedbacks highlighted a better response of the marine component with respect to the terrestrial one, being the land carbon sinks still in the low end of the CMIP6 multi-model variability.

To evaluate the performance of the CMCC-ESM2, key climate and biogeochemical quantities simulated in the historical experiment were compared with available observation-based products. The model reproduces the historical warming trend as well the increase in oceanic heat content and stratification conditions, whereas the sea ice over the Arctic region was significantly underestimated since the early stage of the simulation. However, future climate projections for major physical quantities embeds a number of features, such as the increased precipitation at high latitudes and stratification across the southern hemisphere, that are consistent with IPCC AR5 and SROCC reports.

The evaluation of the land carbon and nitrogen cycles exhibited satisfactory results with values lying in the upper range or slightly above the available observation estimates and coherent with the outcomes of other CMIP6 models, for example, high values of BNF. The 21st century evolution of soil organic carbon is influenced by projected land-use pathways similar to other CMIP6 models. Besides, the different regional biases emerging from the comparison with observational data are expected to be altered by the land-use changes characterizing each future projection. Despite the fair representation of the biogeochemical land cycles in CMCC-ESM2, some carbon and nitrogen pools and fluxes, such as the soil nitrogen pool and ecosystem respiration, require further investigation and future model development.

The assessment of marine biogeochemical cycles showed a reliable comparison with available observations for major inorganic macronutrients and carbon related quantities, with deviations similar to other CMIP6 models, for example, related to the Southern Ocean nutrients trapping and the limited extension of oxygen minimum zones. These biases are very likely to persist over the long-term scenarios and they should be adequately accounted in the evaluation of potential ecosystem impacts, for example, at the regional scale. Despite the coherence in simulated future pH and oxygen conditions with CMIP ensembles, the future projections of net primary production represent a major source of uncertainty that needs to be addressed in the next developments of the model, with potential improvements deriving also from better constrained satellite-based estimates.

CMCC-ESM2 provides a valuable contribution to the CMIP6 ESM diversity in the representation of coupled global climate-carbon dynamics. Future efforts will sustain the improvement of both physical and biogeochemical processes to better constrain long-term environmental responses to anthropogenic drivers and provide an extensive support to the climate community endeavor.

Appendix A: BFM Features for CMIP6 Experiments

The BFM configuration implemented in CCMC-ESM2 can be considered of intermediate complexity (Table A1), having a lower trophic level pelagic ecosystem composed by heterotrophic bacteria, two phytoplanktonic (diatoms and nano-flagellates) and two zooplanktonic (micro- and meso-zooplankton) functional groups. Bacterial and zooplanktonic groups are modeled in terms of the sole carbon constituent with fixed stoichiometric ratios. The benthic compartment response is obtained with a simple but effective scheme that explicitly resolves the benthic intake of particulate organic matter from the water column and the return flux of inorganic nutrients determined by prescribed remineralization rates (see e.g., Soetaert et al., 2000), including also the organic matter burial toward deeper sediment layers as in Dunne et al. (2007).

With respect to the previous CMIP5 model version, the cycling of dissolved iron is here extended to include the effect of (a) dust particle dissolution also below the ocean surface layer (Moore et al., 2004) and (b) sedimentary inputs prescribed over a three dimensional representation of seabed area fractions (details in Aumont & Bopp, 2006), with a constant iron flux set to $1 \mu\text{molFe m}^{-2} \text{d}^{-1}$. Although complex chemistry modules were

recently developed (e.g., Aumont et al., 2015), a simple formulation was here preferred to limit the cost of including further oceanic tracers in the model. Thus, the temperature-dependent iron regeneration from organic matter components of Vichi et al. (2011) was revised with a first order scavenging process over free inorganic iron (Parekh et al., 2004).

$$\frac{\partial N_f}{\partial t} = k_f^{\text{ing}} \cdot (N_f - N_f^{\text{LIG}}), \quad (\text{A1})$$

where k_f^{ing} is the inorganic scavenging rate (0.01 d^{-1}), N_f is the dissolved inorganic iron concentration, and N_f^{LIG} is the uniform total ligand concentration (0.6 nM), and a second order scavenging depending on the concentration of organic particulate matter (Parekh et al., 2005).

$$\frac{\partial N_f}{\partial t} = k_f^{\text{org}} \cdot N_f \cdot R_c^\alpha, \quad (\text{A2})$$

with k_f^{org} as the organic scavenging rate ($1.58\text{e}-5 \text{ d}^{-1}$), α is a constant coefficient (0.58), and R_c the particulate organic matter concentration.

To improve the turnover dynamics of dissolved silica over the wide range of seawater temperatures encountered at the global scale, the temperature dependent dissolution of particulate organic silica was modified to use the exponential Arrhenius formulation (Sarmiento & Gruber, 2006) as in the following:

$$k = k_{\text{Si}} \cdot \frac{E_a}{R} \cdot \left(\frac{1}{T_{\text{ref}}} - \frac{1}{T} \right), \quad (\text{A3})$$

where k_{Si} indicates the reference dissolution rate (0.001 d^{-1}), E_a is the activation energy (60 J mol^{-1}), R is the universal gas constant, and T_{ref} and T are the reference (10°C) and local seawater temperatures, respectively.

A major change with respect to the reference BFM version 5.2 (Vichi et al., 2020) is here represented by a new conceptual framework to describe the heterotrophic bacteria growth dynamics and interactions with the different organic matter components. The growth of marine heterotrophic bacteria is largely controlled by seawater temperature and substrate availability (Pomeroy & Wiebe, 2001), but with several implications arising from the environmental distribution of the latter. In fact, these two regulating factors are equally relevant in the case of bacterial organisms suspended in the water column, while on particulate organic matter bacteria are known to form attached colonies that primarily grow according to the substrate concentration. By assuming that bacteria biomass (B) distributes between dissolved (R_s), and particulate organic matter (R_a) with a linear proportion of their carbon content, namely $\varphi_R = R_s / (R_s + R_a)$, the partitioned biomasses can be expressed as $B_s = B \cdot \varphi_R$ and $B_a = B \cdot (1 - \varphi_R)$. The whole bacterial community gross growth will be then obtained by the summation of the specific contribution from suspended organisms growth

$$\frac{\partial B_s}{\partial t} = \mu \cdot f_B^T \cdot \left(\frac{R_s^3}{R_s^3 + X_s^3} \right) \cdot B_s \quad (\text{A4})$$

with the one from colonies attached to particulate matter

$$\frac{\partial B_a}{\partial t} = \mu \cdot f_B^P \cdot \left(\frac{R_a^3}{R_a^3 + (X_a \cdot B_a)^3} \right) \cdot B_a \quad (\text{A5})$$

where μ is the specific growth rate (3.0 d^{-1}), f_B^T is the temperature regulating factor ($Q_{10} = 2.95$), f_B^P is regulating factor due to vertical pressure, and X_a and X_s are the respective half-saturation coefficients set to $1,000$ and 50 mgC m^{-3} . Following the theoretical scheme from Wang and Li (2014), the interaction of bacteria with organic matter substrates can be described through the classic Monod equation for suspended living organisms, while the Contois formulation is used for attached colonies where the bacterial biomass becomes the main regulating factor. A steep cubic sigmoid was used to represent the enhanced bacterial response under optimal conditions and its sudden lowering when limitation factors become more relevant. The bacterial biomass partition between the two organic matter components introduces an implicit exchange of microbial organisms between suspended and attached phases. The regulating term f_B^P addresses the reduction of bacterial activity under increasing pressure levels as highlighted by recent observations on the change of the bacterial assemblage composition across

ocean depths (Grossart & Gust, 2009; Thiele et al., 2015). This effect was parameterized here using a power function, similar to the so-called “Martin curve” (Martin et al., 1987), which provides a straightforward empirical representation of bacterial variation in response to depth (reference depth value is 400 m).

The organic matter by-products of bacterial activity due to both mortality and stoichiometric ratios balance closure are returned to the associated substrate fraction. Note that the uptake and release of inorganic nutrients to maintain fixed stoichiometric ratios, when bacteria are represented only through their carbon content, is obtained by considering the nutritional content of the ingested organic matter. Similarly to Polimene et al. (2006), a refractory dissolved carbon component was included in the model and is released as a fixed fraction of the ingested carbon content. In fact, bacterial activity degrades the structure of organic matter into refractory compounds that could be responsible for a significant sequestration of fixed carbon exported toward the ocean interior (Ogawa et al., 2001). Respiration, mortality, and predation dynamics uses the same formulations of the previous BFM global ocean applications (BACT1 in Vichi et al., 2020), with the exception of nitrate consumption under anaerobic conditions that is computed using a constant carbon to nitrogen ratio (0.86 from Paulmier et al., 2009) instead of the reduction equivalent formulation from Vichi et al. (2004). A simple aggregation scheme of dissolved organic matter into the particulate pool was also included in the model to mimic the interaction between suspended and settling material, which is based on a linear relationship with particulate organic matter concentration occurring at a rate of 2×10^{-3} days.

Table A1
List of All Living and Non-Living Functional Groups Accounted for in the Pelagic and Benthic Compartments of BFM CMIP6 Implementation

Functional group	Component(s)	Constituent(s)
Dissolved inorganic chemicals	Nitrate	N
	Ammonia	N
	Phosphate	P
	Silicate	Si
	Iron	Fe
	Oxygen	O
Bacterioplankton	Heterotrophic Bacteria	C (fixed stoichiometry)
Phytoplankton	Diatoms	C, N, P, Si, and Fe
	Autotrophic Nano-flagellates	C, N, P, and Fe
Zooplankton	Microzooplankton	C (fixed stoichiometry)
	Mesozooplankton	C (fixed stoichiometry)
Pelagic Detritus	Labile Dissolved Organic Matter (DOM)	C, N, P, and Fe
	Particulate Organic Matter (POM)	C, N, P, Si, and Fe
	Refractory Dissolved Organic Matter	C
Carbonate Chemistry	Dissolved inorganic carbon	C
	Total alkalinity	–
Benthic Detritus	Dissolved Organic Matter	C, N, and P
	Particulate Organic Matter	C, N, P, and Si

Note. The constituents column reports all compounds explicitly simulated by each model’s component among carbon (C), nitrogen (N), phosphorous (P), silicate (Si), iron (Fe), and oxygen (O).

Data Availability Statement

All of the CMCC-ESM2 model outputs used in this work are made available for download through the ESGF infrastructure under CMIP6 project.

Acknowledgments

This work was supported by the European Union's Horizon 2020 Research and Innovation Program with the CRESCENDO project under the grant agreement No 641816 and PRIMAVERA project under the grant agreement No 641727. The authors are grateful to the CMCC Super-Computing Center team for the support given during the production of CMIP6 simulations and the publication of model data on ESGF.

References

- Alessandri, A. (2006). *Effects of land surface and vegetation processes on the climate simulated by an atmospheric general circulation model* (PhD Thesis, p. 114). Bologna University Alma Mater Studiorum.
- Arora, V. K., Katavouta, A., Williams, R. G., Jones, C. D., Brovkin, V., Friedlingstein, P., et al. (2020). Carbon-concentration and carbon-climate feedbacks in CMIP6 models and their comparison to CMIP5 models. *Biogeosciences*, *17*(16), 4173–4222. <https://doi.org/10.5194/bg-17-4173-2020>
- Aumont, O., & Bopp, L. (2006). Globalizing results from ocean in situ iron fertilization studies. *Global Biogeochemical Cycles*, *20*(2). <https://doi.org/10.1029/2005GB002591>
- Aumont, O., Éthé, C., Tagliabue, A., Bopp, L., & Gehlen, M. (2015). PISCES-v2: An ocean biogeochemical model for carbon and ecosystem studies. *Geoscientific Model Development*, *8*(8), 2465–2513. <https://doi.org/10.5194/gmd-8-2465-2015>
- Batjes, N. H. (2014). Total carbon and nitrogen in the soils of the world. *European Journal of Soil Science*, *65*(1), 10–21. https://doi.org/10.1111/ejss.12114_2
- Bertolini, T., Flechard, C. R., Fattore, F., Nicolini, G., Stefani, P., Matera, S., et al. (2016). DRY and BULK atmospheric nitrogen deposition to a West-African humid forest exposed to terrestrial and oceanic sources. *Agricultural and Forest Meteorology*, *218*, 184–195. <https://doi.org/10.1016/j.agrformet.2015.12.026>
- Bonan, G. B., Lawrence, P. J., Oleson, K. W., Levis, S., Jung, M., Reichstein, M., et al. (2011). Improving canopy processes in the Community Land Model version 4 (CLM4) using global flux fields empirically inferred from FLUXNET data. *Journal of Geophysical Research*, *116*(G2). <https://doi.org/10.1029/2010JG001593>
- Bond-Lamberty, B., & Thomson, A. (2010). Temperature-associated increases in the global soil respiration record. *Nature*, *464*(7288), 579–582. <https://doi.org/10.1038/nature08930>
- Bowden, R. D., Nadelhoffer, K. J., Boone, R. D., Melillo, J. M., & Garrison, J. B. (1993). Contributions of aboveground litter, belowground litter, and root respiration to total soil respiration in a temperate mixed hardwood forest. *Canadian Journal of Forest Research*, *23*(7), 1402–1407. <https://doi.org/10.1139/x93-177>
- Busecke, J. J., Resplandy, L., & Dunne, J. P. (2019). The equatorial undercurrent and the oxygen minimum zone in the Pacific. *Geophysical Research Letters*, *46*(12), 6716–6725. <https://doi.org/10.1029/2019GL082692>
- Carvalho, N., Forkel, M., Khomik, M., Bellarby, J., Jung, M., Migliavacca, M., et al. (2014). Global covariation of carbon turnover times with climate in terrestrial ecosystems. *Nature*, *514*(7521), 213–217. <https://doi.org/10.1038/nature13731>
- Cherchi, A., Fogli, P. G., Lovato, T., Peano, D., Iovino, D., Gualdi, S., et al. (2019). Global mean climate and main patterns of variability in the CMCC-CM2 coupled model. *Journal of Advances in Modeling Earth Systems*, *11*(1), 185–209. <https://doi.org/10.1029/2018MS001369>
- Cleveland, C. C., Townsend, A. R., Schimel, D. S., Fisher, H., Howarth, R. W., Hedin, L. O., et al. (1999). Global patterns of terrestrial biological nitrogen (N₂) fixation in natural ecosystems. *Global Biogeochemical Cycles*, *13*(2), 623–645. <https://doi.org/10.1029/1999GB900014>
- CMCC. (2020). Climate change in the future fast changing world. The CMCC vision towards 2029. Strategic Plan 2019–2029 (p.94). Retrieved from https://www.cmcc.it/wp-content/uploads/2020/06/Strategic_Plan_v13-1.pdf
- Collatz, G. J., Ribas-Carbo, M., & Berry, J. A. (1992). Coupled photosynthesis-stomatal conductance model for leaves of C₄ plants. *Functional Plant Biology*, *19*(5), 519–538. <https://doi.org/10.1071/PP9920519>
- Craig, A. P., Vertenstein, M., & Jacob, R. (2012). A new flexible coupler for earth system modeling developed for CCSM4 and CESM1. *International Journal of High Performance Computing Applications*, *26*(1), 31–42. <https://doi.org/10.1177/1094342011428141>
- Davies-Barnard, T., & Friedlingstein, P. (2020). The global distribution of biological nitrogen fixation in terrestrial natural ecosystems. *Global Biogeochemical Cycles*, *34*(3), e2019GB006387. <https://doi.org/10.1029/2019GB006387>
- Davies-Barnard, T., Meyerholt, J., Zaehle, S., Friedlingstein, P., Brovkin, V., Fan, Y., et al. (2020). Nitrogen cycling in CMIP6 land surface models: Progress and limitations. *Biogeosciences*, *17*(20), 5129–5148. <https://doi.org/10.5194/bg-17-5129-2020>
- Del Grosso, S. J., Parton, W. J., Mosier, A. R., Ojima, D. S., Kulmala, A. E., & Phongpan, S. (2000). General model for N₂O and N₂ gas emissions from soils due to denitrification. *Global Biogeochemical Cycles*, *14*(4), 1045–1060. <https://doi.org/10.1029/1999GB001225>
- Deutsch, C., Brix, H., Ito, T., Frenzel, H., & Thompson, L. (2011). Climate-forced variability of ocean hypoxia. *Science*, *333*(6040), 336–339. <https://doi.org/10.1126/science.1202422>
- Dickson, A. G. (2010). The carbon dioxide system in seawater: Equilibrium chemistry and measurements. *Guide to best practices for ocean acidification research and data reporting*, *1*, 17–40.
- Dunne, J. P., Sarmiento, J. L., & Gnanadesikan, A. (2007). A synthesis of global particle export from the surface ocean and cycling through the ocean interior and on the seafloor. *Global Biogeochemical Cycles*, *21*(4), GB40006. <https://doi.org/10.1029/2006GB002907>
- Duteil, O., Oschlies, A., & Böning, C. W. (2018). Pacific Decadal Oscillation and recent oxygen decline in the eastern tropical Pacific Ocean. *Biogeosciences*, *15*(23), 7111–7126. <https://doi.org/10.5194/bg-15-7111-2018>
- ETH Zürich (ETHZ). (2017). *input4MIPs.IACETH.aerosolProperties.CMIP.IACETH-SAGE3lambda-3-0-0* (Version 20171006). Earth System Grid Federation. <https://doi.org/10.22033/ESGF/input4MIPs.1681>
- Eyring, V., Bony, S., Meehl, G. A., Senior, C. A., Stevens, B., Stouffer, R. J., & Taylor, K. E. (2016). Overview of the Coupled Model Inter-comparison Project phase 6 (CMIP6) experimental design and organization. *Geoscientific Model Development*, *9*(5), 1937–1958. <https://doi.org/10.5194/gmd-9-1937-2016>
- Farquhar, G. D., von Caemmerer, S. V., & Berry, J. A. (1980). A biochemical model of photosynthetic CO₂ assimilation in leaves of C₃ species. *Planta*, *149*(1), 78–90. <https://doi.org/10.1007/BF00386231>
- Fasullo, J. T., Tomas, R., Stevenson, S., Otto-Bliesner, B., Brady, E., & Wahl, E. (2017). The amplifying influence of increased ocean stratification on a future year without a summer. *Nature Communications*, *8*(1), 1–10. <https://doi.org/10.1038/s41467-017-01302-z>
- Fetterer, F., Knowles, K., Meier, W. N., Savoie, M., & Windnagel, A. K. (2017). *Sea Ice Index, version 3. Sea ice extent for 1979–2014*. NSIDC: National Snow and Ice Data Center. <https://doi.org/10.7265/N5K072F8>
- Firestone, M. K., & Davidson, E. A. (1989). Microbiological basis of NO and N₂O production and consumption in soil. *Exchange of Trace Gases Between Terrestrial Ecosystems and the Atmosphere*, *47*, 7–21.
- Frajka-Williams, E., Moat, B. I., Smeed, D., Rayner, D., Johns, W. E., Baringer, M. O., et al. (2020). *Atlantic Meridional Overturning Circulation observed by the RAPID-MOCHA-WBTS (RAPID-Meridional Overturning Circulation and Heatflux Array-Western Boundary Time Series) array at 26N from 2004 to 2020 (v2020.1)*. British Oceanographic Data Centre, NERC. <https://doi.org/10.5285/cc1e34b3-3385-662b-e053-6c86abc03444>
- Friedlingstein, P., Cox, P., Betts, R., Bopp, L., von Bloh, W., Brovkin, V., et al. (2006). Climate-carbon cycle feedback analysis: Results from the C4MIP model intercomparison. *Journal of Climate*, *19*(14), 3337–3353. <https://doi.org/10.1175/JCLI3800.1>

- Friedlingstein, P., O'Sullivan, M., Jones, M. W., Andrew, R. M., Hauck, J., Olsen, A., et al. (2020). Global Carbon Budget 2020. *Earth System Science Data*, 12(4), 3269–3340. <https://doi.org/10.5194/essd-12-3269-2020>
- Frölicher, T. L., Rodgers, K. B., Stock, C. A., & Cheung, W. W. (2016). Sources of uncertainties in 21st century projections of potential ocean ecosystem stressors. *Global Biogeochemical Cycles*, 30(8), 1224–1243. <https://doi.org/10.1002/2015GB005338>
- Garcia, H. E., Weathers, K., Paver, C. R., Smolyar, I., Boyer, T. P., Locarnini, R. A., et al. (2018a). World Ocean Atlas 2018, volume 4: Dissolved inorganic nutrients (phosphate, nitrate and nitrate+nitrite, silicate). In A. Mishonov (Ed.), (Technical Ed.), *NOAA Atlas NESDIS* (Vol. 84, p. 35).
- Garcia, H. E., Weathers, K., Paver, C. R., Smolyar, I., Boyer, T. P., Locarnini, R. A., et al. (2018b). World Ocean Atlas 2018, volume 3: Dissolved oxygen, apparent oxygen utilization, and oxygen saturation. In A. Mishonov (Ed.), (Technical Ed.), *NOAA Atlas NESDIS* (Vol. 83, p. 38).
- GEOTRACES Intermediate Data Product Group. (2021). *The GEOTRACES Intermediate Data Product 2021 (IDP2021)*. NERC EDS British Oceanographic Data Centre NOC. <https://doi.org/10.5285/cf2d9ba9-d51d-3b7c-e053-8486abc0f5fd>
- Gidden, M., Riahi, K., Smith, S., Fujimori, S., Luderer, G., Krieger, E., et al. (2018). *input4MIPs.CMIP6.ScenarioMIP.IAMC* (Version 20180628). Earth System Grid Federation. <https://doi.org/10.22033/ESGF/input4MIPs.10464>
- Gillett, N. P., Arora, V. K., Matthews, D., & Allen, M. R. (2013). Constraining the ratio of global warming to cumulative CO₂ emissions using CMIP5 simulations. *Journal of Climate*, 26(18), 6844–6858. <https://doi.org/10.1175/JCLI-D-12-00476.1>
- Gregory, J. M., & Forster, P. M. (2008). Transient climate response estimated from radiative forcing and observed temperature change. *Journal of Geophysical Research*, 113(D23). <https://doi.org/10.1029/2008JD010405>
- Gregory, J. M., Ingram, W. J., Palmer, M. A., Jones, G. S., Stott, P. A., Thorpe, R. B., et al. (2004). A new method for diagnosing radiative forcing and climate sensitivity. *Geophysical Research Letters*, 31(3), L03205. <https://doi.org/10.1029/2003GL018747>
- Grossart, H. P., & Gust, G. (2009). Hydrostatic pressure affects physiology and community structure of marine bacteria during settling to 4000 m: An experimental approach. *Marine Ecology Progress Series*, 390, 97–104. <https://doi.org/10.3354/meps08201>
- Gualdi, S., Scoccimarro, E., & Navarra, A. (2008). Changes in tropical cyclone activity due to global warming: Results from a high-resolution coupled general circulation model. *Journal of Climate*, 21(20), 5204–5228. <https://doi.org/10.1175/2008JCLI1921.1>
- Hegglin, M., Kinnison, D., & Lamarque, J.-F. (2018). *input4MIPs.CMIP6.ScenarioMIP.NCAR* (Version 20161207 and 20181112). Earth System Grid Federation. <https://doi.org/10.22033/ESGF/input4MIPs.10465>
- Hegglin, M., Kinnison, D., Lamarque, J.-F., & Plummer, D. (2016). *input4MIPs.CMIP6.CMIP.UReading* (Versions 20160830 and 20180525). Earth System Grid Federation. <https://doi.org/10.22033/ESGF/input4MIPs.10452>
- Hoesly, R., Smith, S., Feng, L., Klimont, Z., Janssens-Maenhout, G., Pitkanen, T., et al. (2016). *input4MIPs.CMIP6.CMIP.PNNL-JGCRI* (Version 20170907). Earth System Grid Federation. <https://doi.org/10.22033/ESGF/input4MIPs.10450>
- Huffman, G. J., Behrangi, A., Bolvin, D. T., & Nelkin, E. J. (2020). *GPCP version 3.1 satellite-gauge (SG) combined precipitation data set* (In G. J. Huffman, A. Behrangi, D. T. Bolvin, & E. J. Nelkin Eds.). NASA GES DISC. <https://doi.org/10.5067/DBVUO4KQHXTK>
- Hunke, E. C., Lipscomb, W. H., Turner, A. K., Jeffery, N., & Elliott, S. (2008). *CICE: The Los Alamos sea ice model, documentation and software user's manual* (p. 87545). T-3 Fluid Dynamics Group, Los Alamos National Laboratory.
- Hurttt, G., Chini, L., Sahajpal, R., Frolking, S., Bodirsky, B. L., Calvin, K., et al. (2019). *Harmonization of global land use change and management for the period 2015-2300* (Version 20190805). Earth System Grid Federation. <https://doi.org/10.22033/ESGF/input4MIPs.10468>
- IPCC. (2013). Climate change 2013: The physical science basis. Contribution of Working Group I to the Fifth Assessment Report of the Intergovernmental Panel on Climate Change. (In T. F. Stocker, D. Qin, G.-K. Plattner, M. Tignor, S. K. Allen, J. Boschung et al., Eds., p. 1535). Cambridge University Press.
- IPCC. (2014). Climate change 2014: Synthesis report. Contribution of working groups I, II and III to the fifth assessment report of the intergovernmental panel on climate change. (In Core Writing Team, R. K. Pachauri, & L. A. Meyer Eds., p. 151). IPCC.
- IPCC. (2019). IPCC Special Report on the Ocean and Cryosphere in a changing climate. (In H.-O. Pörtner, D. C. Roberts, V. Masson-Delmotte, P. Zhai, M. Tignor, E. Poloczanska, et al. Eds.).
- Ito, A., Hajima, T., Lawrence, D. M., Brovkin, V., Delire, C., Guenet, B., et al. (2020). Soil carbon sequestration simulated in CMIP6-LUMIP models: Implications for climatic mitigation. *Environmental Research Letters*, 15(12), 124061. <https://doi.org/10.1088/1748-9326/abc912>
- Joiner, J., & Yoshida, Y. (2021). *Global MODIS and FLUXNET-derived daily gross primary production*, V2. ORNL DAAC.
- Jones, C. D., Arora, V., Friedlingstein, P., Bopp, L., Brovkin, V., Dunne, J., et al. (2016). C4MIP—the coupled climate–carbon cycle model intercomparison project: Experimental protocol for CMIP6. *Geoscientific Model Development*, 9(8), 2853–2880. <https://doi.org/10.5194/gmd-9-2853-2016>
- Jones, C. D., & Friedlingstein, P. (2020). Quantifying process-level uncertainty contributions to TCRE and carbon budgets for meeting Paris Agreement climate targets. *Environmental Research Letters*, 15(7), 074019. <https://doi.org/10.1088/1748-9326/ab858a>
- Juckles, M., Taylor, K. E., Durack, P. J., Lawrence, B., Mizielinski, M. S., Pamment, A., et al. (2020). The CMIP6 data request (DREQ, version 01.00.31). *Geoscientific Model Development*, 13(1), 201–224. <https://doi.org/10.5194/gmd-13-201-2020>
- Jung, M., Reichstein, M., Margolis, H. A., Cescatti, A., Richardson, A. D., Arain, M. A., et al. (2011). Global patterns of land-atmosphere fluxes of carbon dioxide, latent heat, and sensible heat derived from eddy covariance, satellite, and meteorological observations. *Journal of Geophysical Research*, 116(G3). <https://doi.org/10.1029/2010JG001566>
- Kim, H. (2017). *Global soil wetness project phase 3 atmospheric boundary conditions (experiment 1)* (Data set). Data Integration and Analysis System (DIAS). <https://doi.org/10.20783/DIAS.501>
- Koven, C. D., Riley, W. J., Subin, Z. M., Tang, J. Y., Torn, M. S., Collins, W. D., et al. (2013). The effect of vertically resolved soil biogeochemistry and alternate soil C and N models on C dynamics of CLM4. *Biogeosciences*, 10(11), 7109–7131. <https://doi.org/10.5194/bg-10-7109-2013>
- Kwiatkowski, L., Torres, O., Bopp, L., Aumont, O., Chamberlain, M., Christian, J. R., et al. (2020). Twenty-first century ocean warming, acidification, deoxygenation, and upper-ocean nutrient and primary production decline from CMIP6 model projections. *Biogeosciences*, 17(13), 3439–3470. <https://doi.org/10.5194/bg-17-3439-2020>
- Landschützer, P., Gruber, N., & Bakker, D. C. (2016). Decadal variations and trends of the global ocean carbon sink. *Global Biogeochemical Cycles*, 30(10), 1396–1417. <https://doi.org/10.1002/2015GB005359>
- Larcher, W. (1995). Photosynthesis as a tool for indicating temperature stress events. In *Ecophysiology of photosynthesis* (pp. 261–277). Springer. https://doi.org/10.1007/978-3-642-79354-7_13
- Lauvset, S. K., Key, R. M., Olsen, A., Heuven, S. V., Velo, A., Lin, X., et al. (2016). A new global interior ocean mapped climatology: The 1 × 1 GLODAP version 2. *Earth System Science Data*, 8(2), 325–340. <https://doi.org/10.5194/essd-8-325-2016>
- Lévy, M., Resplandy, L., Palter, J. B., Couespel, D., & Lachkar, Z. (2021). Role of mixing in ocean biogeochemistry. In A. C. Naveira Garabato & M. P. Meredith (Eds.), *Ocean mixing*. Elsevier.
- Li, F., Levis, S., & Ward, D. S. (2013). Quantifying the role of fire in the Earth system—Part 1: Improved global fire modeling in the community Earth System Model (CESM1). *Biogeosciences*, 10(4), 2293–2314. <https://doi.org/10.5194/bg-10-2293-2013>

- Li, F., Zeng, X. D., & Levis, S. (2012a). A process-based fire parameterization of intermediate complexity in a Dynamic Global Vegetation Model. *Biogeosciences*, 9(7), 2761–2780. <https://doi.org/10.5194/bg-9-2761-2012>
- Li, F., Zeng, X. D., & Levis, S. (2012b). Corrigendum to "A process-based fire parameterization of intermediate complexity in a Dynamic Global Vegetation Model" published in *Biogeosciences*, 9, 2761–2780, 2012. *Biogeosciences*, 9(11), 4771–4772. <https://doi.org/10.5194/bg-9-4771-2012>
- Li, G., Cheng, L., Zhu, J., Trenberth, K. E., Mann, M. E., & Abraham, J. P. (2020). Increasing ocean stratification over the past half-century. *Nature Climate Change*, 10(12), 1116–1123. <https://doi.org/10.1038/s41558-020-00918-2>
- Liu, X., Easter, R. C., Ghan, S. J., Zaveri, R., Rasch, P., Shi, X., et al. (2012). Toward a minimal representation of aerosols in climate models: Description and evaluation in the Community Atmosphere Model CAM5. *Geoscientific Model Development*, 5(3), 709–739. <https://doi.org/10.5194/gmd-5-709-2012>
- Loeb, N. G., Lyman, J. M., Johnson, G. C., Allan, R. P., Doelling, D. R., Wong, T., et al. (2012). Observed changes in top-of-the-atmosphere radiation and upper-ocean heating consistent within uncertainty. *Nature Geoscience*, 5(2), 110–113. <https://doi.org/10.1038/NGEO1375>
- Lovato, T., & Butenschön, M. (2021). *CMCC CMCC-ESM2 model output prepared for CMIP6 OMIP* (Version 20210127). Earth System Grid Federation. <https://doi.org/10.22033/ESGF/CMIP6.13167>
- Lovato, T., & Peano, D. (2020). *CMCC CMCC-CM2-SR5 model output prepared for CMIP6 CMIP piControl* (Version 20200616). Earth System Grid Federation. <https://doi.org/10.22033/ESGF/CMIP6.3874>
- Lovato, T., Peano, D., & Butenschön, M. (2021). *CMCC CMCC-ESM2 model output prepared for CMIP6 C4MIP* (Version 20210301). Earth System Grid Federation. <https://doi.org/10.22033/ESGF/CMIP6.13163>
- Luysaert, S., Inghim, I., Jung, M., Richardson, A. D., Reichstein, M., Papale, D., et al. (2007). CO₂ balance of boreal, temperate, and tropical forests derived from a global database. *Global Change Biology*, 13(12), 2509–2537. <https://doi.org/10.1111/j.1365-2486.2007.01439.x>
- Madec, G., & Imbard, M. (1996). A global ocean mesh to overcome the North Pole singularity. *Climate Dynamics*, 12(6), 381–388. <https://doi.org/10.1007/BF00211684>
- Madec, G., & NEMO System Team. (2016). *Scientific notes of climate modelling center* (p. 27). Institut Pierre-Simon Laplace (IPSL).
- Martin, J. H., Knauer, G. A., Karl, D. M., & Broenkow, W. W. (1987). VERTEX: Carbon cycling in the northeast Pacific. Deep sea research Part A. *Oceanographic Research Papers*, 34(2), 267–285. [https://doi.org/10.1016/0198-0149\(87\)90086-0](https://doi.org/10.1016/0198-0149(87)90086-0)
- Matthes, K., Funke, B., Kruschke, T., & Wahl, S. (2017). *input4MIPs.SOLARIS-HEPPA.solar.CMIP.SOLARIS-HEPPA-3-2* (Version 20170103). Earth System Grid Federation. <https://doi.org/10.22033/ESGF/input4MIPs.1122>
- Mayorga, E., Seitzinger, S. P., Harrison, J. A., Dumont, E., Beusen, A. H., Bouwman, A. F., et al. (2010). Global nutrient export from Water-Sheds 2 (NEWS 2): Model development and implementation. *Environmental Modelling & Software*, 25(7), 837–853. <https://doi.org/10.1016/j.envsoft.2010.01.007>
- Meehl, G. A., Senior, C. A., Eyring, V., Flato, G., Lamarque, J. F., Stouffer, R. J., et al. (2020). Context for interpreting equilibrium climate sensitivity and transient climate response from the CMIP6 Earth System Models. *Science Advances*, 6(26), eaba1981. <https://doi.org/10.1126/sciadv.aba1981>
- Meinshausen, M., & Nicholls, Z. R. J. (2018). *input4MIPs.CMIP6.ScenarioMIP.UoM* (Version 20181127). Earth System Grid Federation. <https://doi.org/10.22033/ESGF/input4MIPs.10467>
- Meinshausen, M., Nicholls, Z. R. J., Lewis, J., Gidden, M. J., Vogel, E., Freund, M., et al. (2020). The shared socio-economic pathway (SSP) greenhouse gas concentrations and their extensions to 2500. *Geoscientific Model Development*, 13(8), 3571–3605. <https://doi.org/10.5194/gmd-13-3571-2020>
- Meinshausen, M., & Vogel, E. (2016). *input4MIPs.UoM.GHGConcentrations.CMIP.UoM-CMIP-1-2-0* (Version 20160830). Earth System Grid Federation. <https://doi.org/10.22033/ESGF/input4MIPs.1118>
- Moore, J. K., Doney, S. C., & Lindsay, K. (2004). Upper ocean ecosystem dynamics and iron cycling in a global three-dimensional model. *Global Biogeochemical Cycles*, 18(4). <https://doi.org/10.1029/2004GB002220>
- Moore, J. K., Fu, W., Primeau, F., Britten, G. L., Lindsay, K., Long, M., et al. (2018). Sustained climate warming drives declining marine biological productivity. *Science*, 359(6380), 1139–1143. <https://doi.org/10.1126/science.aao6379>
- Morice, C. P., Kennedy, J. J., Rayner, N. A., Winn, J. P., Hogan, E., Killick, R. E., et al. (2021). An updated assessment of near-surface temperature change from 1850: The HadCRUT5 data set. *Journal of Geophysical Research: Atmospheres*, 126(3), e2019JD032361. <https://doi.org/10.1029/2019JD032361>
- Myneni, R., Knyazikhin, Y., & Park, T. (2015a). *MOD15A2H MODIS/Terra Leaf Area Index/FPAR 8-day LA Global 500m SIN Grid V006*. NASA EOSDIS Land Processes DAAC. <https://doi.org/10.5067/MODIS/MOD15A2H.006>
- Myneni, R., Knyazikhin, Y., & Park, T. (2015b). *MYD15A2H MODIS/Aqua Leaf Area Index/FPAR 8-day LA Global 500m SIN Grid V006*. NASA EOSDIS Land Processes DAAC. <https://doi.org/10.5067/MODIS/MYD15A2H.006>
- Neale, R. B., Chen, C.-C., Gettelman, A., Lauritzen, P. H., Park, S., Williamson, D. L., et al. (2012). *Description of the NCAR community atmosphere model (CAM 5.0)*. National Center For Atmospheric Research/NCAR/TN-486+ STR.
- Nijse, F. J., Cox, P. M., & Williamson, M. S. (2020). Emergent constraints on transient climate response (TCR) and equilibrium climate sensitivity (ECS) from historical warming in CMIP5 and CMIP6 models. *Earth System Dynamics*, 11(3), 737–750. <https://doi.org/10.5194/esd-11-737-2020>
- Ogawa, H., Amagai, Y., Koike, I., Kaiser, K., & Benner, R. (2001). Production of refractory dissolved organic matter by bacteria. *Science*, 292(5518), 917–920. <https://doi.org/10.1126/science.1057627>
- Oleson, K. W., Lawrence, D. M., Bonan, G. B., Drewniak, B., Huang, M., Koven, C. D., et al. (2013). *Technical description of version 4.5 of the Community Land Model (CLM)* (NCAR Technical Note No. NCAR/TN-503+ STR). National Center for Atmospheric Research.
- O'Neill, B. C., Tebaldi, C., Vuuren, D. P. V., Eyring, V., Friedlingstein, P., Hurtt, G., et al. (2016). The scenario model intercomparison project (ScenarioMIP) for CMIP6. *Geoscientific Model Development*, 9(9), 3461–3482. <https://doi.org/10.5194/gmd-9-3461-2016>
- Orr, J. C., Epitalon, J. M., & Gattuso, J. P. (2015). Comparison of ten packages that compute ocean carbonate chemistry. *Biogeosciences*, 12(5), 1483–1510. <https://doi.org/10.5194/bg-12-1483-2015>
- Orr, J. C., Najjar, R. G., Aumont, O., Bopp, L., Bullister, J. L., Danabasoglu, G., et al. (2017). Biogeochemical protocols and diagnostics for the CMIP6 Ocean Model Intercomparison Project (OMIP). *Geoscientific Model Development*, 10(6), 2169–2199. <https://doi.org/10.5194/gmd-10-2169-2017>
- Papalexioiu, S. M., Rajulapati, C. R., Clark, M. P., & Lehner, F. (2020). Robustness of CMIP6 historical global mean temperature simulations: Trends, long-term persistence, autocorrelation, and distributional shape. *Earth's Future*, 8(10), e2020EF001667. <https://doi.org/10.1029/2020EF001667>
- Parekh, P., Follows, M. J., & Boyle, E. (2004). Modeling the global ocean iron cycle. *Global Biogeochemical Cycles*, 18(1). <https://doi.org/10.1029/2003GB002061>

- Parekh, P., Follows, M. J., & Boyle, E. A. (2005). Decoupling of iron and phosphate in the global ocean. *Global Biogeochemical Cycles*, *19*(2). <https://doi.org/10.1029/2004GB002280>
- Parton, W. J., Holland, E. A., Del Grosso, S. J., Hartman, M. D., Martin, R. E., Mosier, A. R., et al. (2001). Generalized model for NO_x and N₂O emissions from soils. *Journal of Geophysical Research*, *106*(D15), 17403–17419. <https://doi.org/10.1029/2001JD900101>
- Parton, W. J., Mosier, A. R., Ojima, D. S., Valentine, D. W., Schimel, D. S., Weier, K., & Kulmala, A. E. (1996). Generalized model for N₂ and N₂O production from nitrification and denitrification. *Global Biogeochemical Cycles*, *10*(3), 401–412. <https://doi.org/10.1029/96GB01455>
- Parton, W. J., Stewart, J. W., & Cole, C. V. (1988). Dynamics of C, N, P and S in grassland soils: A model. *Biogeochemistry*, *5*(1), 109–131. <https://doi.org/10.1007/BF02180320>
- Paulmier, A., Kriest, I., & Oschlies, A. (2009). Stoichiometries of remineralisation and denitrification in global biogeochemical ocean models. *Biogeosciences*, *6*(5), 923–935. <https://doi.org/10.5194/bg-6-923-2009>
- Peano, D., Hemming, D., Materia, S., Delire, C., Fan, Y., Joetzier, E., et al. (2021). Plant phenology evaluation of CRESCENDO land surface models—Part 1: Start and end of the growing season. *Biogeosciences*, *18*(7), 2405–2428. <https://doi.org/10.5194/bg-18-2405-2021>
- Peano, D., Lovato, T., & Materia, S. (2020a). *CMCC CMCC-ESM2 model output prepared for CMIP6 LS3MIP* (Version 20200225). Earth System Grid Federation. <https://doi.org/10.22033/ESGF/CMIP6.13165>
- Peano, D., Lovato, T., & Materia, S. (2020b). *CMCC CMCC-ESM2 model output prepared for CMIP6 LUMIP* (Version 20200225). Earth System Grid Federation. <https://doi.org/10.22033/ESGF/CMIP6.13166>
- Peano, D., Materia, S., Collalti, A., Alessandri, A., Anav, A., Bombelli, A., & Gualdi, S. (2019). Global variability of simulated and observed vegetation growing season. *Journal of Geophysical Research*, *124*(11), 3569–3587. <https://doi.org/10.1029/2018JG004881>
- Piao, S., Luysaert, S., Ciais, P., Janssens, I. A., Chen, A., Cao, C., et al. (2010). Forest annual carbon cost: A global-scale analysis of autotrophic respiration. *Ecology*, *91*(3), 652–661. <https://doi.org/10.1890/08-2176.1>
- Polimene, L., Pinardi, N., Zavatarelli, M., & Colella, S. (2006). The Adriatic Sea ecosystem seasonal cycle: Validation of a three-dimensional numerical model. *Journal of Geophysical Research*, *111*(C3). <https://doi.org/10.1029/2005jc003260>
- Pomeroy, L. R., & Wiebe, W. J. (2001). Temperature and substrates as interactive limiting factors for marine heterotrophic bacteria. *Aquatic Microbial Ecology*, *23*(2), 187–204. <https://doi.org/10.3354/ame023187>
- Predybaylo, E., Stenichkov, G., Wittenberg, A. T., & Osipov, S. (2020). El Niño/Southern Oscillation response to low-latitude volcanic eruptions depends on ocean pre-conditions and eruption timing. *Communications Earth & Environment*, *1*(1), 1–13. <https://doi.org/10.1038/s43247-020-0013-y>
- Sarmiento, J. L. N., & Gruber (2006). *Ocean Biogeochemical dynamics*. Princeton University Press.
- Sathyendranath, S., Grant, M., Brewin, R. J. W., Brockmann, C., Brotas, V., Chuprin, A., et al. (2018). *ESA ocean colour climate change initiative (Ocean_Colour_cci): Version 3.1 data*. Centre for Environmental Data Analysis. <https://doi.org/10.5285/9c334fbe6d424a708cf3c4cf0c6a53f5>
- Sathyendranath, S., Platt, T., Kovač, Ž., Dingle, J., Jackson, T., Brewin, R. J. W., et al. (2020). Reconciling models of primary production and photoacclimation. *Applied Optics*, *59*(10), C100–C114. <https://doi.org/10.1364/AO.386252>
- Scoccimarro, E., Gualdi, S., Bellucci, A., Sanna, A., Fogli, P. G., Manzini, E., et al. (2011). Effects of tropical cyclones on ocean heat transport in a high-resolution coupled general circulation model. *Journal of Climate*, *24*(16), 4368–4384. <https://doi.org/10.1175/2011JCLI4104.1>
- Séférian, R., Berthet, S., Yool, A., Palmieri, J., Bopp, L., Tagliabue, A., et al. (2020). Tracking improvement in simulated marine biogeochemistry between CMIP5 and CMIP6. *Current Climate Change Reports*, *6*, 95–119. <https://doi.org/10.1007/s40641-020-00160-0>
- Séférian, R., Gehlen, M., Bopp, L., Resplandy, L., Orr, J. C., Marti, O., et al. (2016). Inconsistent strategies to spin up models in CMIP5: Implications for ocean biogeochemical model performance assessment. *Geoscientific Model Development*, *9*(5), 1827–1851. <https://doi.org/10.5194/gmd-9-1827-2016>
- Soetaert, K., Middelburg, J. J., Herman, P. M., & Buis, K. (2000). On the coupling of benthic and pelagic biogeochemical models. *Earth-Science Reviews*, *51*(1–4), 173–201. [https://doi.org/10.1016/S0012-8252\(00\)00004-0](https://doi.org/10.1016/S0012-8252(00)00004-0)
- Tagliabue, A., Aumont, O., DeAth, R., Dunne, J. P., Dutkiewicz, S., Galbraith, E., et al. (2016). How well do global ocean biogeochemistry models simulate dissolved iron distributions? *Global Biogeochemical Cycles*, *30*(2), 149–174. <https://doi.org/10.1002/2015GB005289>
- Tagliabue, A., Kwiatkowski, L., Bopp, L., Butenschön, M., Cheung, W., Lengaigne, M., & Vialard, J. (2021). Persistent uncertainties in ocean net primary production climate change projections at regional scales raise challenges for assessing impacts on ecosystem services. *Frontiers in Climate*, *3*, 1–16. <https://doi.org/10.3389/fclim.2021.738224>
- Taylor, K. E., Stouffer, R. J., & Meehl, G. A. (2012). An overview of CMIP5 and the experiment design. *Bulletin of the American Meteorological Society*, *93*(4), 485–498. <https://doi.org/10.1175/BAMS-D-11-00094.1>
- Tebaldi, C., Debeire, K., Eyring, V., Fischer, E., Fyfe, J., Friedlingstein, P., et al. (2021). Climate model projections from the scenario model intercomparison project (ScenarioMIP) of CMIP6. *Earth System Dynamics*, *12*(1), 253–293. <https://doi.org/10.5194/esd-12-253-2021>
- Thiele, S., Fuchs, B. M., Amann, R., & Iversen, M. H. (2015). Colonization in the photic zone and subsequent changes during sinking determine bacterial community composition in marine snow. *Applied and Environmental Microbiology*, *81*(4), 1463–1471. <https://doi.org/10.1128/AEM.02570-14>
- Thornton, P. E. (1998). *Regional ecosystem simulation: Combining surface and satellite-based observations to study linkages between terrestrial energy and mass budgets*. University of Montana.
- Tsujino, H., Urakawa, L. S., Griffies, S. M., Danabasoglu, G., Adcroft, A. J., Amaral, A. E., et al. (2020). Evaluation of global ocean–sea-ice model simulations based on the experimental protocols of the Ocean Model Intercomparison Project phase 2 (OMIP-2). *Geoscientific Model Development*, *13*(8), 3643–3708. <https://doi.org/10.5194/gmd-13-3643-2020>
- Vichi, M., Lovato, T., Butenschön, M., Tedesco, L., Lazzari, P., Cossarini, G., et al. (2020). *The Biogeochemical Flux Model (BFM): Equation description and user manual. BFM version 5.2* (BFM Report series N. 1, Release 1.2, p. 104). Retrieved from <http://bfm-community.eu>
- Vichi, M., Manzini, E., Fogli, P. G., Alessandri, A., Patara, L., Scoccimarro, E., et al. (2011). Global and regional ocean carbon uptake and climate change: Sensitivity to a substantial mitigation scenario. *Climate Dynamics*, *37*(9), 1929–1947. <https://doi.org/10.1007/s00382-011-1079-0>
- Vichi, M., Pinardi, N., & Masina, S. (2007). A generalized model of pelagic biogeochemistry for the global ocean ecosystem. Part I: Theory. *Journal of Marine Systems*, *64*(1–4), 89–109. <https://doi.org/10.1016/j.jmarsys.2006.03.006>
- Vichi, M., Ruardij, P., & Baretta, J. (2004). Link or sink: A modelling interpretation of the open Baltic biogeochemistry. *Biogeosciences*, *1*(1), 79–100. <https://doi.org/10.5194/bg-1-79-2004>
- Vitousek, P. M., Menge, D. N., Reed, S. C., & Cleveland, C. C. (2013). Biological nitrogen fixation: Rates, patterns and ecological controls in terrestrial ecosystems. *Philosophical Transactions of the Royal Society B: Biological Sciences*, *368*(1621), 20130119. <https://doi.org/10.1098/rstb.2013.0119>
- Wang, Z. W., & Li, Y. (2014). A theoretical derivation of the Contois equation for kinetic modeling of the microbial degradation of insoluble substrates. *Biochemical Engineering Journal*, *82*, 134–138. <https://doi.org/10.1016/j.bej.2013.11.002>
- Waring, R. H., & Running, S. W. (2010). *Forest ecosystems: Analysis at multiple scales*. Elsevier.

- Weijer, W., Cheng, W., Garuba, O. A., Hu, A., & Nadiga, B. T. (2020). CMIP6 models predict significant 21st century decline of the Atlantic Meridional Overturning Circulation. *Geophysical Research Letters*, *47*(12), e2019GL086075. <https://doi.org/10.1029/2019GL086075>
- Wieder, W. R., Lawrence, D. M., Fisher, R. A., Bonan, G. B., Cheng, S. J., Goodale, C. L., et al. (2019). Beyond static benchmarking: Using experimental manipulations to evaluate land model assumptions. *Global Biogeochemical Cycles*, *33*(10), 1289–1309. <https://doi.org/10.1029/2018GB006141>
- Xie, X., Li, A., Jin, H., Tan, J., Wang, C., Lei, G., et al. (2019). Assessment of five satellite-derived LAI datasets for GPP estimations through ecosystem models. *The Science of the Total Environment*, *690*, 1120–1130. <https://doi.org/10.1016/j.scitotenv.2019.06.516>
- Zanna, L., Khatiwala, S., Gregory, J. M., Ison, J., & Heimbach, P. (2019). Global reconstruction of historical ocean heat storage and transport. *Proceedings of the National Academy of Sciences*, *116*(4), 1126–1131. <https://doi.org/10.1073/pnas.1808838115>
- Zeng, N., Mariotti, A., & Wetzol, P. (2005). Terrestrial mechanisms of interannual CO₂ variability. *Global Biogeochemical Cycles*, *19*(1). <https://doi.org/10.1029/2004GB002273>
- Zhu, X., Dong, W., Wei, Z., Guo, Y., Gao, X., Wen, X., et al. (2018). Multi-decadal evolution characteristics of global surface temperature anomaly data shown by observation and CMIP5 models. *International Journal of Climatology*, *38*(3), 1533–1542. <https://doi.org/10.1002/joc.5264>

References From the Supporting Information

- Griffies, S. M., Danabasoglu, G., Durack, P. J., Adcroft, A. J., Balaji, V., Böning, C. W., et al. (2016). OMIP contribution to CMIP6: Experimental and diagnostic protocol for the physical component of the Ocean Model Intercomparison Project. *Geoscientific Model Development*, *9*(9), 3231–3296. <https://doi.org/10.5194/gmd-9-3231-2016>
- Holte, J., Talley, L. D., Gilson, J., & Roemmich, D. (2017). An Argo mixed layer climatology and database. *Geophysical Research Letters*, *44*(11), 5618–5626. <https://doi.org/10.1002/2017GL073426>
- Locarnini, R. A., Mishonov, A. V., Baranova, O. K., Boyer, T. P., Zweng, M. M., et al. (2018). World Ocean Atlas 2018, volume 1: Temperature. In A. Mishonov (Ed.), (Technical Ed.), *NOAA Atlas NESDIS* (Vol. 81, p. 52).
- Zweng, M. M., Reagan, J. R., Seidov, D., Boyer, T. P., Locarnini, R. A., et al. (2018). World Ocean Atlas 2018, volume 2: Salinity. In A. Mishonov (Ed.), (Technical Ed.), *NOAA Atlas NESDIS* (Vol. 82, p. 50).